

RESEARCH ARTICLE

10.1002/2016JD025319

Key Points:

- Agricultural fires smoke confined to the PBL with large optical depth (~3 at 500 nm) and absorption
- A heavy air pollution affected by the transported smoke with ground PM₁₀ and PM_{2.5} reaching 800 μg/m³ and 485 μg/m³
- WRF-Chem model partially captures high PM_{2.5} event but shows a discrepancy due to improper vertical apportionment and transport timing

Supporting Information:

- Supporting Information S1

Correspondence to:

Y. Han,
HanYong@nju.edu.cn

Citation:

Wu, Y., Y. Han, A. Voulgarakis, T. Wang, M. Li, Y. Wang, M. Xie, B. Zhuang, and S. Li (2017), An agricultural biomass burning episode in eastern China: Transport, optical properties, and impacts on regional air quality, *J. Geophys. Res. Atmos.*, 122, 2304–2324, doi:10.1002/2016JD025319.

Received 4 MAY 2016

Accepted 23 JAN 2017

Accepted article online 25 JAN 2017

Published online 16 FEB 2017

An agricultural biomass burning episode in eastern China: Transport, optical properties, and impacts on regional air quality

Yonghua Wu¹ , Yong Han² , Apostolos Voulgarakis³ , Tijian Wang² , Mengmeng Li² , Yuan Wang², Min Xie², Bingling Zhuang², and Shu Li² 

¹NOAA-CREST, City College of the City University of New York, New York, New York, USA, ²School of Atmospheric Science, Nanjing University, Nanjing, China, ³Department of Physics, Imperial College London, London, UK

Abstract Agricultural biomass burning (ABB) has been of particular concern due to its influence on air quality and atmospheric radiation, as it produces large amounts of gaseous and aerosol emissions. This paper presents an integrated observation of a significant ABB episode in Nanjing, China, during early June 2011, using combined ground-based and satellite sensors (Moderate Resolution Imaging Spectroradiometer, Atmospheric Infrared Sounder, Cloud-Aerosol Lidar and Infrared Pathfinder Satellite Observation (CALIPSO), and Ozone Monitoring Instrument products). The time-height distribution, optical properties, sources and transport of smoke, and its impacts on air quality are investigated. Lidar profiles indicate that the smoke aerosols are confined to the planetary boundary layer (PBL) and have a depolarization ratio of less than 0.08. The aerosol optical depths increase from 0.5 to 3.0 at 500 nm, while the extinction-related Angstrom exponent increases from 1.1 to 1.6 at the wavelength pair of 440–870 nm. The single-scattering albedo becomes lower at 670–1020 nm following the ABB intrusion and particularly shows a decreasing tendency between wavelengths of 440 to 1020 nm. The absorption Angstrom exponent (0.7) is smaller than 1.0, which may indicate the aged smoke particles mixed or coated with the urban aerosols. Surface particular matter PM₁₀ and PM_{2.5} show a dramatic increase, reaching hourly mean of 800 μg/m³ and 485 μg/m³, respectively, which results in a heavy air pollution event. The stagnant and high-moisture weather provides favorable conditions for the aerosols to accumulate near the surface. Cloud-Aerosol Lidar and Infrared Pathfinder Satellite Observation (CALIPSO) also illustrate that the large-scale aerosols are primarily present in the PBL and transported to the ocean, but some dense smoke plumes are misclassified as cloud or polluted dust. By comparing with the observations, we found that the Weather Research and Forecasting–Chemistry model captured the accumulation and downwind transport of surface PM_{2.5} from 20:00 on 2 June to 10:00 on 3 June (phase 1) but showed a dramatic underestimate from 20:00 on 3–4 June (phase 2) when dense aerosols are present. Such a discrepancy in the model is associated with the improper vertical apportionment of transported smoke and atmospheric diffusion conditions when comparing with the observed aerosol and wind profiles. In addition, the model simulations indicate that the transported smoke can contribute to 50–70% of the ground-level PM_{2.5} in Nanjing.

1. Introduction

ABB or open fires emit large amounts of smoke aerosols and trace gases, thus affecting air quality and climate on local, regional, and continental scales [Voulgarakis and Field, 2015; Voulgarakis et al., 2015]. The emissions include aerosols (or particular matter PM_{2.5} and PM₁₀ with particle diameters <2.5 μm and 10 μm, respectively), specifically black carbon (BC) and organic carbon (OC), as well as gases, such as carbon monoxide (CO), carbon dioxide (CO₂), and nitrogen oxides (NO_x) [Li et al., 2010; Qu et al., 2012; Zha et al., 2013; Ni et al., 2015; Zhang et al., 2015]. Although some regulations have been applied by the Chinese agencies to prevent straw open fires in agricultural harvest seasons (early summer and fall), field-based burnings of crop residues remain widespread across large parts of China and result in heavy air pollution featuring hazy skies [Qu et al., 2012; Zhang et al., 2015]. Streets et al. [2003] and Yan et al. [2006] estimated that 17–25.6% of total agricultural residue or 110–157.5 Tg of crop waste were burned in the field in China every year. Xia et al. [2013] found that crop fires enhanced aerosol optical depth (AOD), CO, and NO₂ amounts near sources and in downwind regions by ~15–60% in mideastern China. Cheng et al. [2014] indicate that formation of secondary inorganic particles can be intensified due to interaction of smoke with urban/industrial

pollutants in an urban environment. Wang *et al.* [2015a] showed that under high relative humidity and southerly winds, fire emissions from straw burning combined with high urban/industrial emissions to produce intensive regional haze pollution in the North Plain of China.

Smoke aerosols can affect cloud microphysics, radiation, and precipitation by providing cloud condensation nuclei (CCN) and absorbing/scattering solar radiation [Andreae *et al.*, 2004]. Carbonaceous aerosols (BC or elemental carbon (EC) and organic carbon (OC)) in agricultural fire smoke generally absorb more sunlight [Bond and Bergstrom, 2006; Giles *et al.*, 2012]. Thus, when absorbing smoke aerosols mix with low clouds, there is generally a reduction in cloud cover owing to absorption of solar energy in the aerosol layer, thereby cooling the surface, heating the atmosphere, and increasing stability [Ackerman *et al.*, 2000; Koren *et al.*, 2004]. However, smoke aerosols may also serve as CCN, then invigorate clouds, and increase cloud fraction and height (a result of the microphysical effects) when the aerosol loading is not high enough [Andreae *et al.*, 2004; Koren *et al.*, 2008]. In addition, when smoke is overlaying the low cloud decks, their absorption of sunlight can enhance the strength of inversion capping the boundary layer, thereby inhibiting cloud top entrainment, leading to a thickening of the cloud deck and allowing the cloud liquid water path to increase [Johnson *et al.*, 2004].

Chemistry-transport models (CTMs) and chemistry-climate models (CCMs) are increasingly used to quantify biomass burning aerosol transport and effects on air quality and climate. Uncertainties in model estimates result from the emission magnitude, plume vertical distribution, and absorption properties, as well as lack of observational constraints [National Research Council, 2009]. For instance, Ni *et al.* [2015] indicated that the BC emission of agricultural fires depends on whether a fire is flaming or smoldering, and the increase of moisture in the wheat straw increases the emission factors (EFs) of CO, OC, and PM_{2.5}, probably a result of the enhanced smoldering burn of wet fuel. Zhang *et al.* [2015] recently found that the contribution of BC to PM_{2.5} mass is as high as 50% in the flaming phase of some burns due to the reduced amount of OC (and therefore total PM_{2.5}), whereas during smoldering it can decrease to a few percent. Therefore, the aerosols may have a lower single-scattering albedo (SSA) and lower total mass in the flaming phase, and thus, the absorption aerosol optical depth (AAOD) is not necessarily higher than the one in the smoldering phase. Furthermore, aerosol mass extinction efficiency (MEE) is an important parameter for modeling aerosol radiative effects and for remote sensing of air quality (e.g., using satellite-derived AOD to estimate PM_{2.5}) [Hand and Malm, 2007; Hoff and Christopher, 2009], but it varies much with aerosol microphysical/chemical properties and moisture. Carbonaceous aerosols remain a major “wild card” in understanding recent climate change, with highly uncertain direct, indirect, and semidirect effects. Sato *et al.* [2003] found that several models underestimated BC (OC) absorption relative to Aerosol Robotic Network (AERONET) by a factor of 2–4 (1.5–2) globally.

Several episodes of agricultural fire smoke and its effects on local air quality have been observed in the Nanjing area, based on surface in situ and satellite observations [Zhu *et al.*, 2011; Chen *et al.*, 2014; Cheng *et al.*, 2014]. To our best knowledge, there is still a lack of measurements of the time-height distribution and optical characteristics of smoke aerosols for such cases, particularly of optical properties such as single-scattering albedo and absorption spectral dependence. In addition, the large-scale and range-resolved distribution of smoke aerosols and the model performance need to be evaluated for assessing their regional transport and environmental effects. The goal of this study is to fill these gaps by using the integrated ground-based lidar, Sun photometer, and satellite remote sensing observations. The paper is organized as follows: the instruments, data, and methodology are described in section 2; section 3 presents and discusses the observation results. The Weather Research and Forecasting–Chemistry (WRF–Chem) modeled ground-level PM_{2.5} and meteorological parameters are evaluated by comparison to our integrated measurements. A short summary is presented in section 4.

2. Instruments, Data, and Methodology

2.1. Ground-Based Instruments

A synergistic suite of ground-based observing facilities is deployed on the roof of a 24-story building on the Gulou campus of Nanjing University (Urban Atmospheric Environments Observation Station; 32.05°N, 118.78°E; 94 m above sea level (asl)). This includes a polarization-sensitive Raman-Mie lidar (PRML), a CIMEL Sun photometer (CE-318), a visibility sensor (model GSN-1), an aethalometer (model AE-31), and an automatic air

quality monitoring station, analyzing in situ samples for PM₁₀ and PM_{2.5} (TEOM Particulate Mass Monitor Series 1400) and gases (NO_x, Hg, CO₂/CO, and SO₂). The observation site is centrally located in the main urban area of Nanjing City, which is the second largest city in East China, and features a high population density and large energy consumption. East China, including the middle and lower reaches of the Yangtze River and Yellow River, is a major agricultural region that includes about one third of China's cultivated land and almost half of the country's agricultural yields [Huang *et al.*, 2012].

A polarization-sensitive Raman-Mie lidar (PRML) provides the time-height distribution of aerosols, extinction coefficient, and total depolarization ratio; the planetary boundary layer (PBL) height can also be inferred according to the sharp gradient of backscattering signals [Xie *et al.*, 2008; Wu *et al.*, 2010]. It is equipped with a linearly polarized laser source (neodymium: yttrium/aluminum/garnet) pointed vertically, emitting a pulse of 120 mJ output energy at a wavelength of 532 nm and with a 10 Hz repetition rate. The optical receiver is a Cassegrain telescope with 22 cm diameter and a field of view of 0.5–2 mrad. Three receiving channels are used to collect elastic scattering and polarization signals (532 parallel and 532 perpendicular channels) and N₂-Raman scattering signals at 607 nm. The range resolution is 7.5 m, and the lidar is set to automatically collect the data for 8 min average every 30 min. Raman lidar permits independent retrieval of aerosol extinction and backscatter in the night, while the elastic-scattering signal is used to retrieve aerosol extinction in the daytime. Total linear depolarization ratio is obtained from the ratio of the perpendicular polarization component to the parallel component of the backscattered signals [Sassen, 1991], which is a useful indicator of particle nonsphericity for discriminating aerosol types. Generally, smoke and industrial particles are spherical with small depolarization ratio, whereas dust and cirrus clouds are nonspherical in shape, thus exhibiting large depolarization ratio.

A co-located CIMEL Sun/sky radiometer (CE-318) is used to obtain AOD at 340–1640 nm and extinction-related Angstrom exponent (EAE), the latter providing information on particle size (the larger the AE, the smaller the particle size) that helps discriminate fine-mode particles such as smoke and industrial aerosols from coarse-mode dust particles [Giles *et al.*, 2012; Wu *et al.*, 2012]. This is the same model of Sun photometer as used in AERONET [Holben *et al.*, 1998], and the AERONET algorithms are applied to derive aerosol optical properties. The primary product of the Sun photometer is AOD, which is calculated from solar extinction at eight of the nominal wavelengths (340, 380, 440, 500, 675, 870, 1020, and 1640 nm). The water vapor retrieval is derived from the 940 nm channel. A cloud-screening algorithm is applied to remove cloud contamination of the measurements, which results in an aerosol product generally considered as level 1.5. The uncertainty of measured AOD is 0.01–0.02 [Dubovik and King, 2000]. Additionally, the single-scattering albedo (SSA) of aerosol can be retrieved from the almucantar mode measurement, and then absorption AOD and its spectral dependence (i.e., absorption Angstrom exponent or AAE) can be derived [Dubovik and King, 2000; Russell *et al.*, 2010]. For “pure” BC in the atmosphere, the AAE is assumed to be 1 [Bond and Bergstrom, 2006] and observations of AAE > 1 are often taken as evidence of brown carbon (BrC) or dust.

Meanwhile, a visibility sensor (model GSN-1) is deployed to monitor visibility based on the Koschmider principle [Horvath and Noll, 1969], and the aerosol extinction coefficient at 500 nm can then be inferred. Surface PM_{2.5} and PM₁₀ concentrations are continuously monitored and recorded as hourly averages. PM_{2.5} is usually referred to as fine particles, while particles with diameters between 2.5 and 10 μm are referred to as coarse-mode particles. Thus, the aerosol mass extinction efficiency (ratio of aerosol extinction coefficient to mass concentration of PM_{2.5}) can be estimated.

2.2. Satellite Products

To investigate aerosol transport and regional-scale spatial distribution, the satellite products from NASA Moderate Resolution Imaging Spectroradiometer (MODIS) and Cloud-Aerosol Lidar and Infrared Pathfinder Satellite Observation (CALIPSO) are used. The MODIS instrument is on board the Terra and Aqua satellites and provides AOD and Angstrom exponent measurements, which are retrieved from the “Dark Target” algorithm over land and the “Deep Blue” algorithm over bright deserts [Levy *et al.*, 2007]. The level 3 AOD and AE (collection 5.1, spatial resolution 1 × 1°) are used in this study [Levy *et al.*, 2007]. Han *et al.* [2015b] compared MODIS-AOD data with Sun photometer measurements in Nanjing and found a high correlation and a linear regression slope close to 1.0. Regionally, a good agreement between MODIS and AERONET AOD retrievals was found, with the correlation coefficient ranging from 0.82 to 0.89 in Yangtze Delta

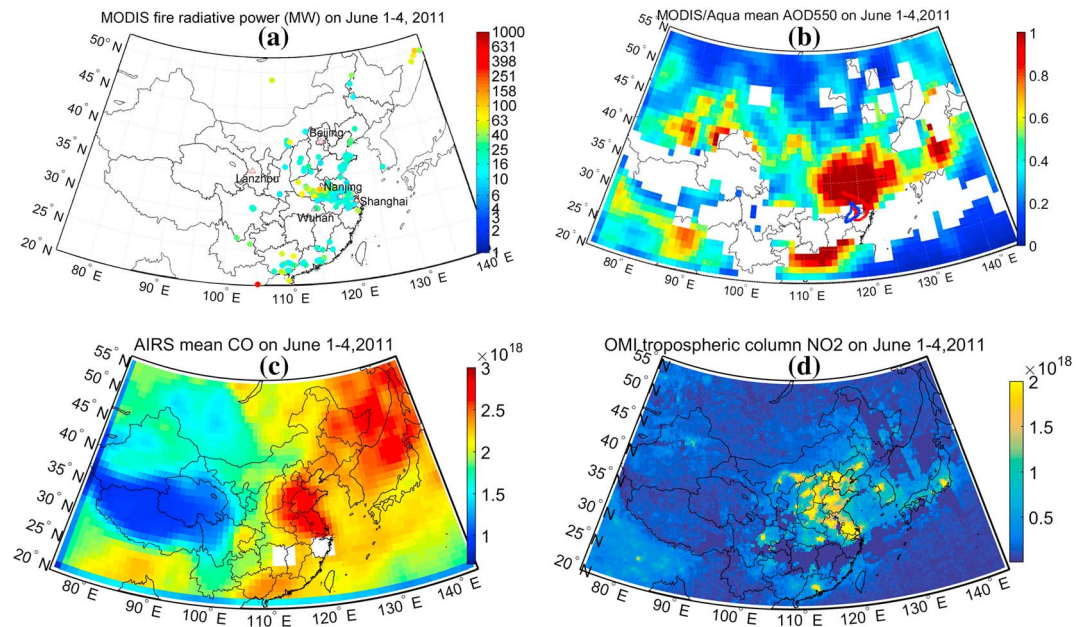


Figure 1. (a) Fire radiative power (FRP), (b) AOD from MODIS, (c) CO from AIRS, and (d) NO₂ from OMI in China during 1–4 June 2011. The thick red and blue curves in Figure 1b are the air backward trajectories with the ending point at Nanjing, 00:00 on 3 June (red) and 4 June (blue), 48 h long at 1 km altitude.

region [Pan *et al.*, 2010]. The Fire Information for Resource Management System delivers global MODIS hot spots/fire locations. Active fire locations correspond to the center of a 1 km pixel that is flagged by the MOD14/MYD14 Fire and Thermal Anomalies algorithm as containing one or more hot spots/fires within the pixel (<https://firms.modaps.eosdis.nasa.gov/>). The MODIS active fire products include the fire radiative power product (FRP), a measure of fire intensity. Integrating the FRP over the lifetime of the fire provides an estimate of the total fire radiative energy, which, for wildfires, should be proportional to the total mass of fuel biomass combusted, thus potentially permitting improved estimates of pyrogenic gaseous and aerosol emissions [Giglio *et al.*, 2006].

CO from the Atmospheric Infrared Sounder (AIRS) satellite and NO₂ from the Ozone Monitoring Instrument (OMI) satellite are used to study the effects of emissions from crop burning on gaseous composition. AIRS version 5, L2 total column CO concentration is derived from the 4.55 μm region of AIRS spectra [Suskind *et al.*, 2003]. The data are available at <http://disc.sci.gsfc.nasa.gov/AIRS>. The OMI-derived tropospheric vertical NO₂ column densities are used to track potential enhancement of NO₂ pollution from crop burning [Boersma *et al.*, 2001]. The level 3 daily NO₂ product has a spatial resolution of 0.25 × 0.25° latitude-longitude.

The Cloud-Aerosol Lidar with Orthogonal Polarization, on board the CALIPSO platform, is a spaceborne polarization-sensitive two-wavelength (532 and 1064 nm) lidar [Winker *et al.*, 2009]. It observes the global aerosol/cloud vertical distribution and provides products of aerosol-type classification and optical properties. In this study, level 1 attenuated backscatters, linear volume depolarization ratio, and level 2 aerosol extinction are used.

2.3. WRF-Chem Model

The Weather Research and Forecasting–Chemistry model (WRF-Chem) version 3.7 is used to simulate meteorology and atmospheric composition over Nanjing [Grell *et al.*, 2005; Wang *et al.*, 2012; Huang *et al.*, 2012, 2013; Xie *et al.*, 2015]. It is an online three-dimensional, Eulerian chemical-transport model that considers the complex atmospheric physical and chemical processes. In this study, it is configured with one domain centered at 31°N and 118°E covering eastern China with horizontal grid resolution of 12 km × 12 km. Twenty-four vertical layers are spaced unequally from the ground to 50 hPa, with eight layers (model full-σ levels are 1.0, 0.993, 0.983, 0.97, 0.954, 0.934, 0.909, and 0.88) located below 1 km to resolve the boundary layer. The National Centers for Environmental Prediction (NCEP)/Final meteorological data are used to initialize each model

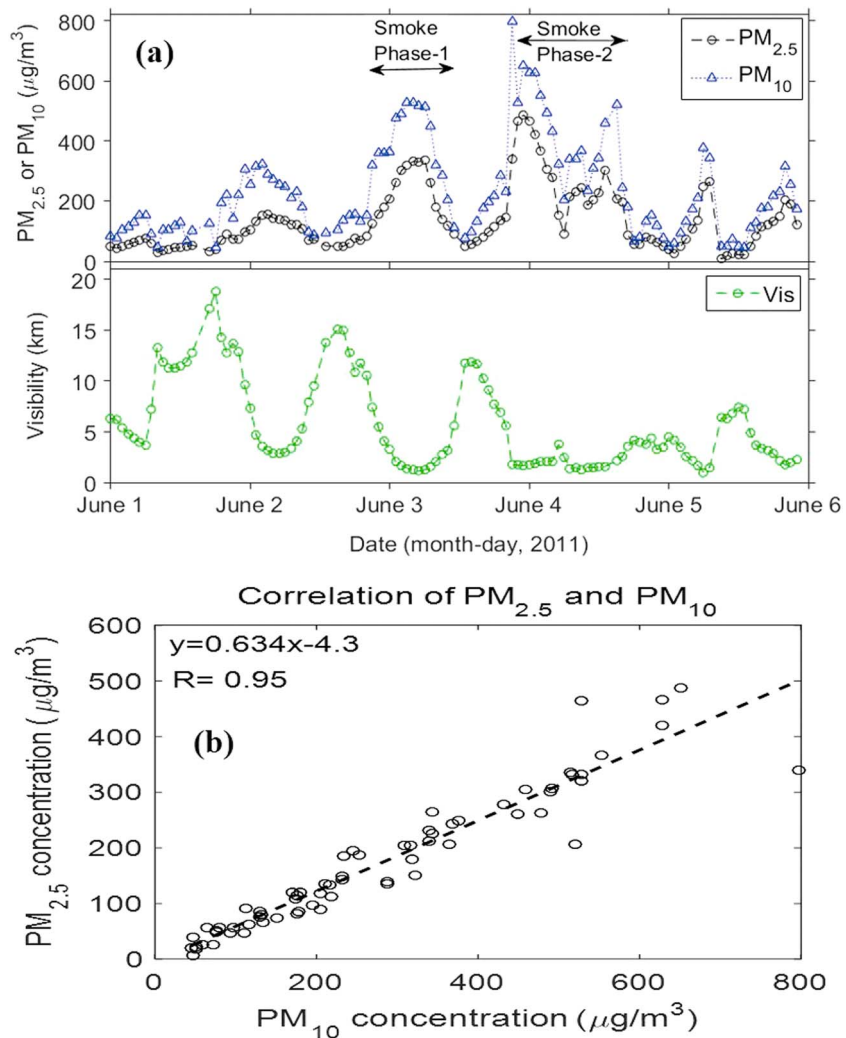


Figure 2. (a) Ground PM₁₀, PM_{2.5}, and visibility. (b) Correlation between PM₁₀ and PM_{2.5} at the Gulou site on 1–5 June 2011.

iteration. The chemical initial conditions are provided by the predictions of the previous model cycle. A 12 h spin-up time is allowed for each 60 h model cycle to minimize the influence of initial conditions [Berge *et al.*, 2001]. We use the Multiresolution Emission Inventory for China, which includes major anthropogenic sources (power plant, industry, agriculture, transportation, and residential fuel) (<http://www.meicmodel.org/>), and the biogenic VOC emissions are calculated online using the Model of Emissions of Gases and Aerosols from Nature model [Guenther *et al.*, 2006]. The inventory for emissions from open-field biomass burning is compiled with a spatial resolution of 1 km based on province-level statistical data and the MODIS fire product [Huang *et al.*, 2012]. The crop fire emissions are occurring on the first model level; thus, no plume-rise parameterization is considered. The diurnal variation of crop fire emissions is specified, and more details can be found in Huang *et al.* [2012]. The model includes the Carbon-Bond Mechanism version Z (CBM-Z) gas-phase chemical mechanism and the Model for Simulating Aerosol Interactions and Chemistry (MOSAIC) aerosol module with four size bins. The CBM-Z contains 55 prognostic species and 134 reactions [Zaveri and Peters, 1999]. In MOSAIC, the aerosol size distribution is divided into either four or eight discrete size bins for various aerosols covering a dry diameter range of 0.059–10 μm [Zaveri *et al.*, 2008]. Aerosol direct and indirect effects through interaction with atmospheric radiation, photolysis, and microphysic routines are also taken into account. The physical parameterized options contain the Noah land surface scheme [Ek *et al.*, 2003], the Lin microphysics scheme [Lin *et al.*, 1983], the Grell cumulus scheme [Grell and Devenyi, 2002], the Yonsei University boundary layer scheme [Noh *et al.*, 2003], the Goddard short-wave radiation scheme [Chou and

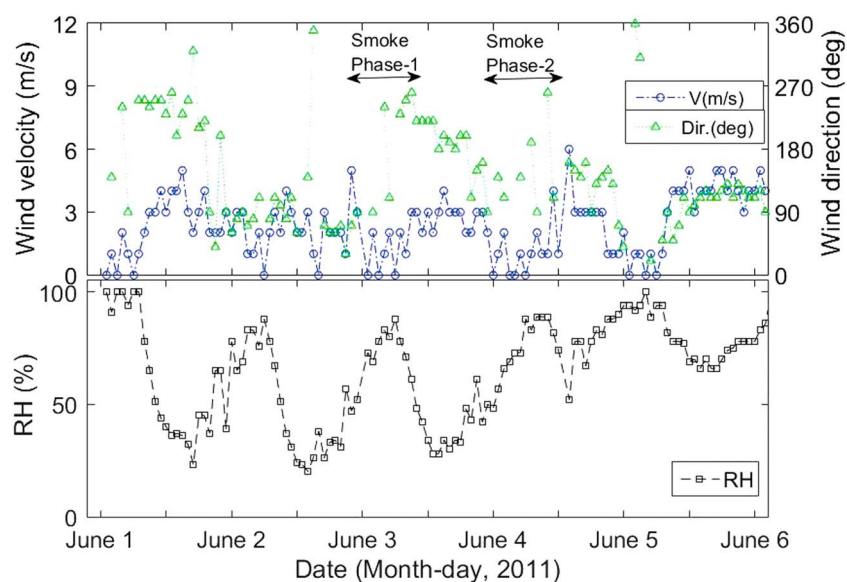


Figure 3. Surface wind speed and relative humidity (RH) in Nanjing during 1–5 June 2011.

Suarez, 1999], the Rapid Radiative Transfer Model long-wave radiation scheme [Gallus and Bresch, 2006], and the Monin-Obukhov surface similarity scheme [Monin and Obukhov, 1954].

In addition, the NOAA–Hybrid Single-Particle Lagrangian Integrated Trajectory (HYSPLIT) model is used to compute air parcel trajectories and to model the dispersion and the route of dust particles [Draxler and Hess, 1997]. For this, input weather maps of the pressure and wind fields are provided by the National Centers for Environmental Prediction (NCEP) reanalysis data.

3. Results and Discussion

3.1. Agricultural Biomass Burning Sources, Emissions, and Transport

Figure 1a shows the fire radiative power (FRP) from the MODIS product during 1–4 June 2011. As it can be seen, there are many fires occurring in mideastern China, a major agricultural region where farmers burn the wheat straw or residue after agricultural harvest at the end of May to fertilize the soil for the upcoming maize crop. The agricultural open fires were reported by the local agencies (<http://news.sohu.com/20110604/n309311426.shtml>). The AOD from MODIS/Aqua shown in Figure 1b reaches values greater than 1.0, representing high loadings of aerosol particles in eastern China. Meanwhile, both the CO and NO₂ columns in Figures 1c and 1d also show high concentrations and similar spatial patterns with the AOD in eastern China, indicating the large emissions from the agricultural open fires and anthropogenic sources. In addition, the air backward trajectories (thick curves in Figure 1b) from the NOAA-HYSPLIT model are given for a 48 h long period at 1 km altitude ending at Nanjing, 00:00 3–4 June, which generally indicates the occurrence of air transport path from the fire sources to Nanjing.

3.2. Impacts on Air Quality and Visibility

Figure 2 shows the time series of PM₁₀, PM_{2.5}, and visibility at the Gulou site. High levels of PM₁₀ and PM_{2.5} mass are indicated on 3–4 June, with peak values of 800 μg/m³ and 485 μg/m³, respectively. Two periods with large PM_{2.5} increase can be seen: phase 1 from 20:00, 2 June to 10:00, 3 June and phase 2 from 20:00, 3 June to 16:00, 4 June. These values are much larger than the Chinese national air quality standard of 75 μg/m³ for PM_{2.5}, thus can be defined as a heavy air pollution episode. The visibility decreases from 15 km to 1 km and clearly shows an inverse relationship with the PM_{2.5} concentrations. Meanwhile, Figure 2b shows a good correlation between PM_{2.5} and PM₁₀, with the linear regression slope indicating the mean fraction of PM_{2.5} in the PM₁₀ mass (63%). Meanwhile, PM₁₀ and PM_{2.5} measurements from another site at Caochangmen (30 m asl; 1.5 km away from the Gulou site) show similar temporal variation and magnitude with those at the Gulou site (see Figures S1 and S2 in the supporting information). Cheng et al. [2014]

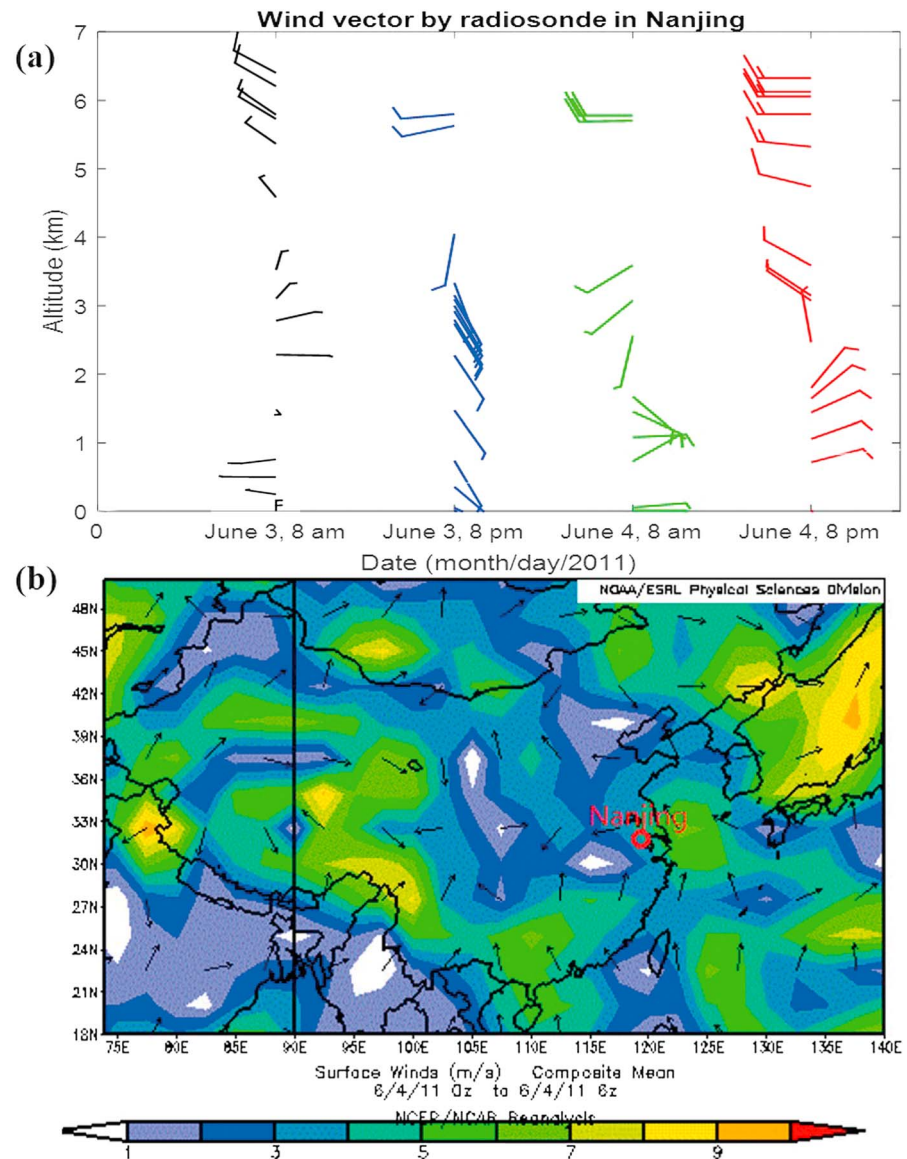


Figure 4. (a) Wind profiles from radiosonde on 3–4 June at Nanjing. (b) NCEP reanalysis surface winds over China on 4 June 2011 (red circle: Nanjing).

and Lu *et al.* [2014] analyzed the daily aerosol composition and found significant increase in OC, BC, and nonsoil or water-soluble potassium K^+ (a good indicator of agricultural biomass burning) on 3–4 June and relatively stable levels of the industrial inorganic SO_4^{2-} , NO_3^- , and NH_4^+ . These results verify the significant influence from agricultural fire smoke.

The surface meteorological conditions shown in Figure 3 generally indicate the light wind (velocity $<3 \text{ ms}^{-1}$) that prevailed during the days of study. By looking at Figures 2a and 3, the time periods of high $PM_{2.5}$ concentrations generally correspond to the prevailing northern or northwestern winds, which transport the ABB smoke to Nanjing on 2–4 June. The low-level $PM_{2.5}$ corresponds to southwesterly or southerly winds. High moisture (relative humidity (RH) $>70\%$) is found during the nights of 2–3 June and for most of the time during 4 June when the $PM_{2.5}$ loadings are also high. These high levels of $PM_{2.5}$ and moisture greatly reduce ground visibility. Furthermore, Figure 4 shows the wind velocities from the radiosonde measurements in Nanjing and indicates that light winds ($<3.5 \text{ m/s}$) prevailed in the PBL below 2 km. The NCEP reanalysis verifies the weak winds and high moisture (RH $>70\%$; not shown here) on 4 June in southeast China in Figure 4. The synoptic weather is under a stable high-pressure system, thus providing favorable conditions

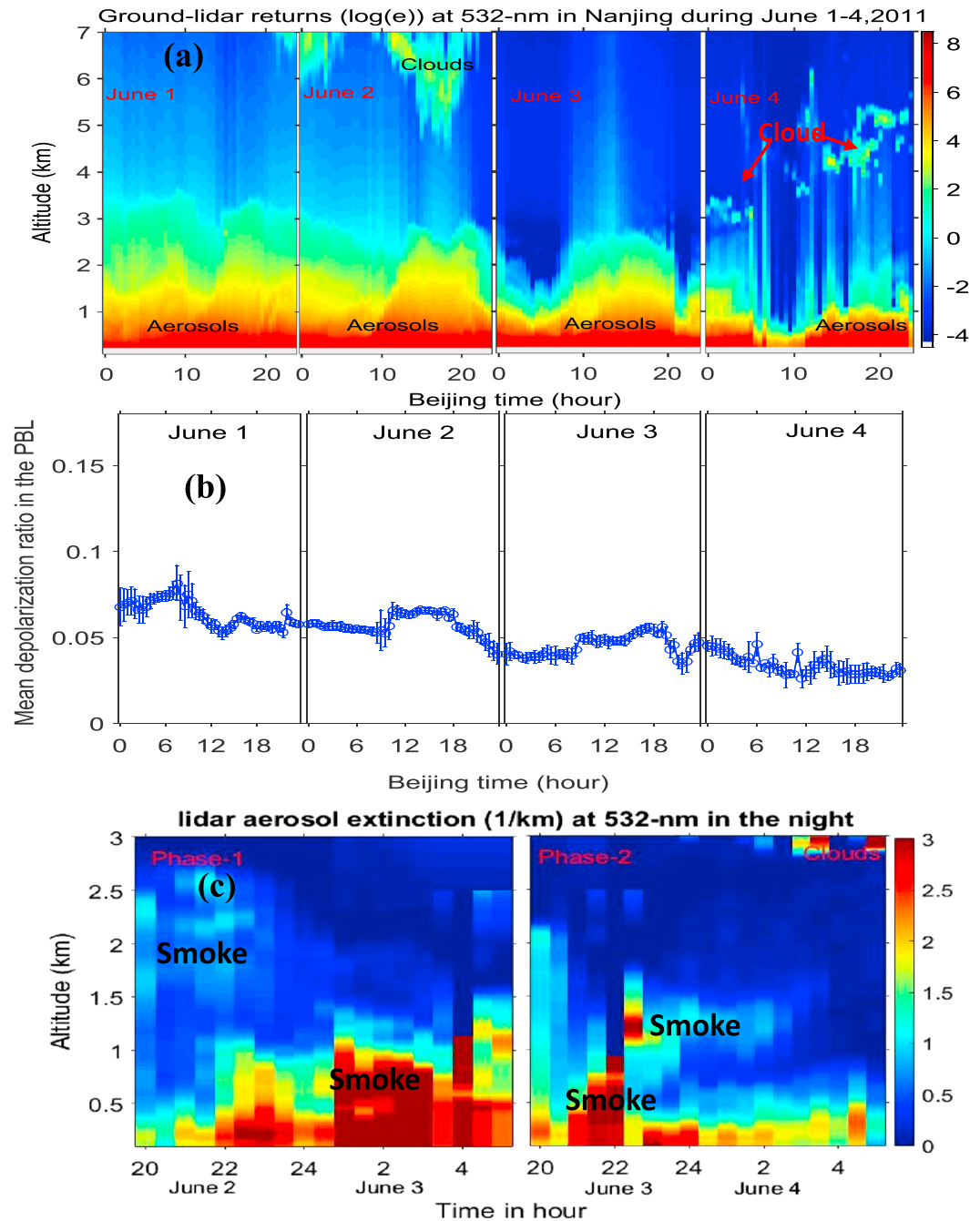


Figure 5. (a) Range-resolved returns of lidar, (b) mean depolarization ratio in the PBL, and (c) aerosol extinction coefficient in phase 1 of smoke intrusion (from 20:00 on 2 June to 5:00 on 3 June) and phase 2 (from 20:00 on 3 June to 5:00 on 4 June).

for aerosol accumulation and a subsequent heavy air pollution episode. Overall, the regional-scale stagnant weather provides favorable conditions for smoke aerosols to accumulate near the surface. Such weather patterns are also verified for other years during the agricultural fire seasons and seriously degrade air quality in Nanjing [Zhu et al., 2011; Qu et al., 2012; Chen et al., 2014].

3.3. Time-Height Distribution and Optical Properties of Aerosols

The time-height distribution, depolarization ratio, and extinction coefficient of aerosols in the PBL from the lidar observations are shown in Figure 5 for 1–4 June. The results indicate that the aerosols are mostly

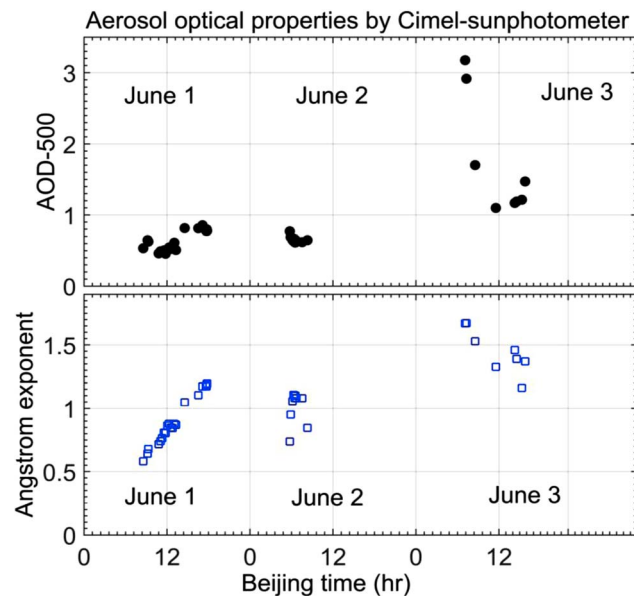


Figure 6. Aerosol optical depth (AOD) and extinction-related Angstrom exponent in Nanjing measured by Sun photometer during 1–3 June 2011.

loaded in the PBL below 1.5 km. In the daytime (10:00–18:00) on 1–3 June, the aerosols can be transported to higher altitudes due to the strong convection, resulting in lower surface $PM_{2.5}$ concentrations. However, on 4 June, most aerosols are trapped below 1 km, which leads to the high levels of $PM_{2.5}$ near the surface; meanwhile the clouds appear at 3–5 km altitude over the whole day of 4 June. The depolarization ratios of the PBL aerosols are relatively small (<0.08), which indicates the dominance of spherical particles. Meanwhile, the aerosol extinction coefficients are retrieved for the time periods of smoke plume intrusions: phase 1 (from 20:00, 2 June to 5:00, 3 June) and phase 2 (from 20:00, 3 June to 5:00, 4 June) when large amounts of $PM_{2.5}$ can be seen in Figure 2. Large aerosol extinctions below 1 km indicate that the smoke transports mainly occur in the PBL below 1 km. In addition, some aloft light aerosols layers appear at 1.5–3 km in the phase 1 and 1–2 km in the phase 2; these aerosols are associated with the transport of the agricultural fire smoke. The lidar ratio is estimated in the range of 46–60 sr at 532 nm below 1 km altitude. Total aerosol optical depth (AOD) and extinction-related Angstrom exponents (EAEs) at 440–87 nm obtained by Sun photometer are shown in Figure 6. As it can be seen, both the AOD and the EAE show a significant increase from 1–2 to 3 June (no retrievals exist for 4 June due to the clouds). The AODs increase from 0.6 to 3.0 at 500 nm, while the EAEs vary from 1.0 to 1.6, indicating more fine-mode particles. Additionally, the single-scattering albedo (SSA) is given in Figure 7a. The SSAs on 3 June become much lower at 670–1020 nm than the ones on other days, indicating strong absorbing properties of aerosols. Particularly, they show a decreasing tendency from 440 to 1020 nm wavelength; this is much different from the increasing tendency that would be expected for dust aerosols [Russell *et al.*, 2010; Han *et al.*, 2015a].

The spectral dependence of aerosol absorption optical depth (AAOD) is given in Figure 7b, from which the absorption Angstrom exponent (AAE) can be estimated. The AAE value for the heavy loading of aerosols on 3 June is 0.70 at the wavelength pair 440–675 nm and 0.55 at 440–870 nm, which is smaller than 1.0 generally for the BC-dominant absorber [Bergstrom *et al.*, 2002]. These values are also much smaller than those on other days (~ 1.46) in Figure 7b and for dust (1.8–2.0) in Nanjing. In contrast, the AAE value for the ABB episode on 3 June is much smaller than those (1.2–1.5) for African biomass burning aerosols [Russell *et al.*, 2010]. Nevertheless, it is consistent with the in situ measurements of 0.5–1.0 at the wavelength pair 467–660 nm in Beijing and Nanjing in the ABB seasons of 2012 and 2013 [Wu *et al.*, 2015; Zhuang *et al.*, 2015]. According to the $PM_{2.5}$ component analysis for this event in Nanjing [Lu *et al.*, 2014], the fractional contributions of daily average OC and BC to the total $PM_{2.5}$ mass are 28.5% and 6.4% on 3 June, respectively, and the sum of inorganic SO_4^{2-} , NO_3^- , and NH_4^+ contributes 20.7% to the total $PM_{2.5}$. Thus, the aged smoke particles (OC and BC) are mixed or coated with other urban aerosols in Nanjing, which probably makes the AAE smaller than 1.0.

The AAE is found to relate to the fire combustion efficiency (smoldering versus flaming), organic matter fraction (OC/BC), particle size and morphology, coating or mixture with other types of aerosols, and moisture [Bergstrom *et al.*, 2002, 2007; Russell *et al.*, 2010; Bahadur *et al.*, 2012; Wu *et al.*, 2015; Garg *et al.*, 2016]. A few observations in the urban cities of China indicate a smaller AAE (see summary in Table S1 in the supporting information). Assuming a spectrally constant index of refraction, very small spherical black carbon particles ($r \approx 0.01 \mu\text{m}$) can have an AAE of 1.0 while larger optically effective black carbon particles (e.g., $r > 0.1 \mu\text{m}$)

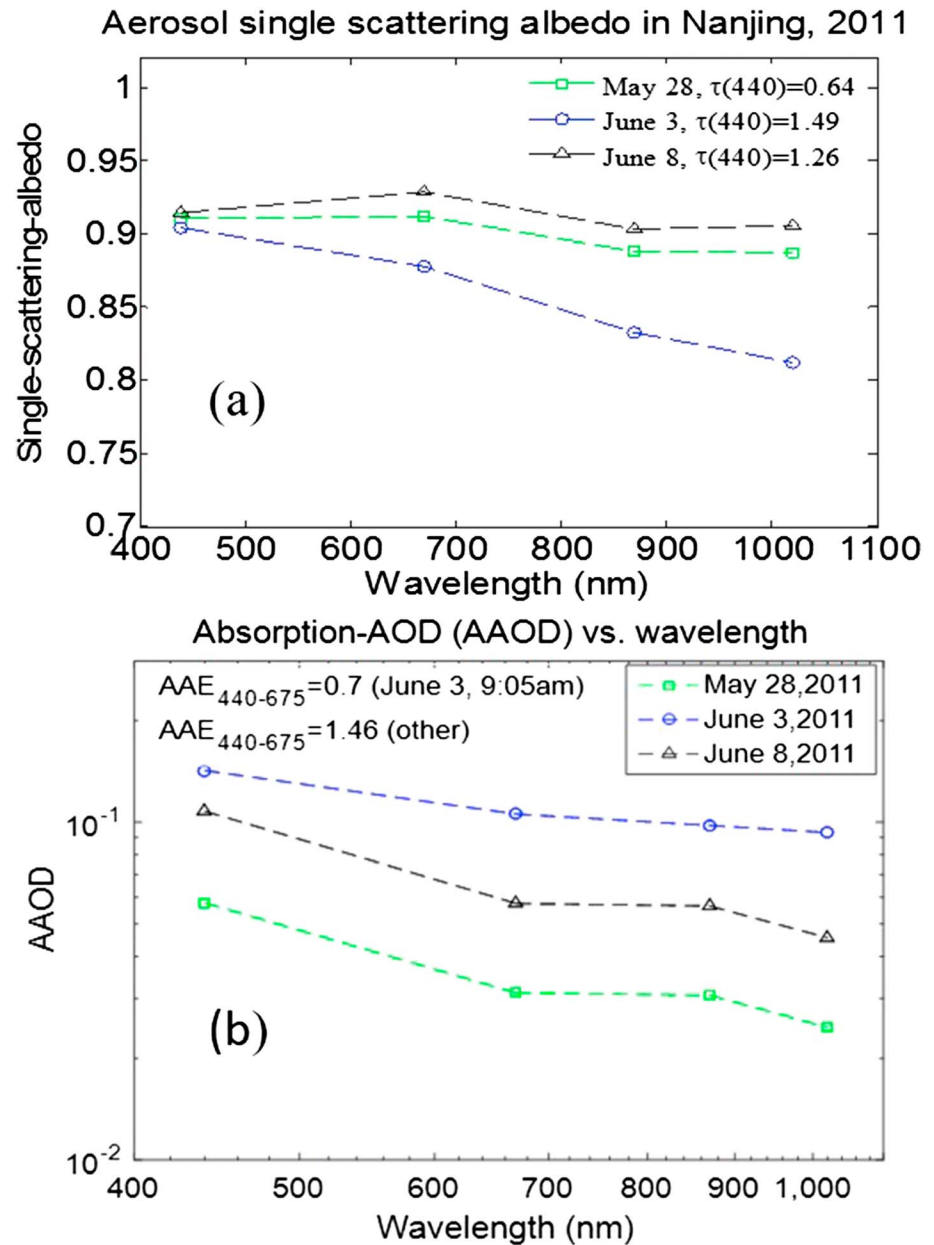


Figure 7. (a) Aerosol single-scattering albedo (SSA) and (b) aerosol absorption optical depth (AAOD) measured by the Sun photometer. $\tau(440)$: AOD at 440 nm, AAE₄₄₀₋₆₇₅: absorption Angstrom exponent at wavelength pair of 440–675 nm.

have AAE values below 1.0 for large cores [Lack and Cappa, 2010]. Wang et al. [2015a] analyzed the aerosol mass size distribution for an ABB event in June 2012 in Beijing, and the results indicate that the maxima of BC and OC mass correspond to particle radii of $r=0.3\ \mu\text{m}$ and $0.45\ \mu\text{m}$, respectively, and the second peak for the mass appears at $r=2\text{--}2.5\ \mu\text{m}$. Wu et al. [2015] found that the AAE was 1–1.2 on clean days but significantly lower than 1 (0.5–0.8) during ABB seasons at the wavelength pair 467–660 nm in Beijing during 28 May to 1 July 2012. The simulation indicates that larger core size and medium coating thickness make the AAE lower. Bahadur et al. [2012] showed that AAE is typically smaller than unity for the biomass burning aerosols in Asia. Larger particles in biomass burning and residential source regions would decrease absorption. In Nanjing, Zhuang et al. [2014] showed that the AAE decreased with increasing RH. In addition, brown carbon (BrC) in eastern Asia outflow has been reported as highly absorbing at long wavelengths (e.g., visible and near-infrared spectrum), which also can result in a low AAE (<1.0) [Alexander et al., 2008; Lack et al., 2012;

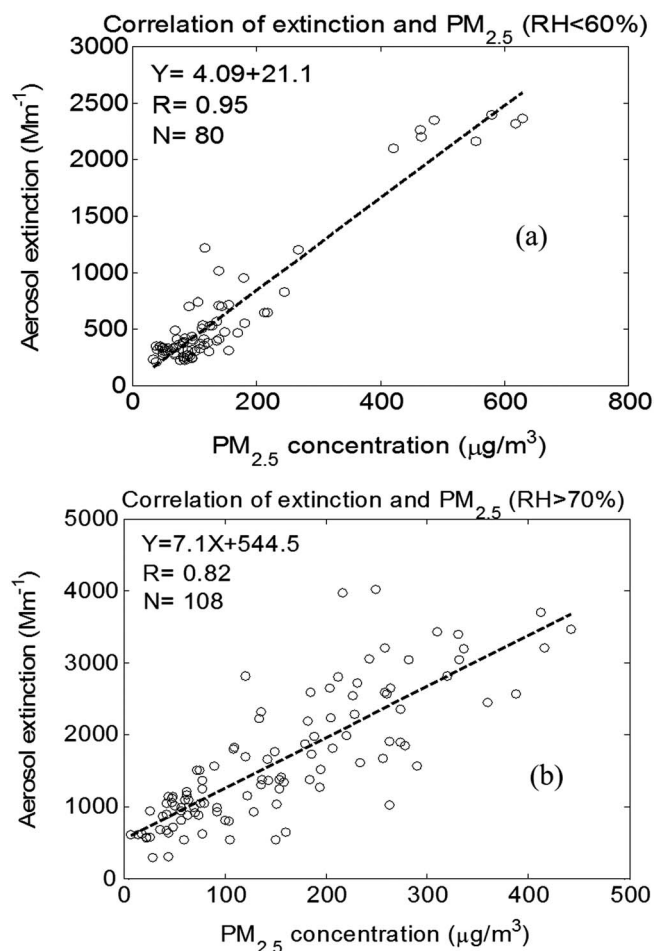


Figure 8. Correlation between aerosol extinction and PM_{2.5}. (a) RH < 60% (dry) and (b) RH > 70% (wet).

ground PM_{2.5} shows good correlation with column AOD with a correlation coefficient of 0.81. This suggests that the AOD can be an indicator of ground PM_{2.5} for this agricultural biomass burning season in Nanjing as the smoke aerosols are mainly located in the PBL. The regression slope over the ABB season is smaller than the one (~95) in the dust season [Han et al., 2015b].

3.4. Regional-Scale Height Distribution of Aerosol in Eastern China

The range-resolved and large-scale distributions and optical properties of aerosols are shown in Figure 9 from CALIPSO satellite measurements at 2:17–2:30 (Beijing time, night) on 3 June 2011. Figure 9a indicates that the aerosols are mainly located below 2.5 km at latitudes of 31°N–37°N (fire regions from the MODIS fire map), and some aloft aerosols appear below 5 km at latitudes of 37°–40°N. The middle to high level of clouds in the south of 31°N and north of 40°N prevents aerosol detection because of the large attenuation by clouds. The depolarization ratios are generally smaller (0.04–0.1) in those agricultural fire regions (31°–37°N and 110°–120°E), but a little higher at 37°–40°N, as shown in Figure 9b. The aerosol extinctions in Figure 10c indicate the larger values (>1.0 km⁻¹ at 532 nm) below 1 km altitude, then following with a transient layer at 1–3 km altitude with the extinction coefficient at 0.1–1.0 km⁻¹. The altitude-integrated AOD is at 1.0–2.0 along the CALIPSO track. This is consistent with the ground lidar retrievals shown in Figure 5c. Furthermore, the aerosols are mostly classified as polluted continental and smoke at the latitude of 31°–37°N, whereas the aloft aerosols are classified as polluted dust and dust at 37°–40°N in the CALIPSO vertical-feature-mask (VFM) product. Please note that some dense aerosols are partly misclassified as clouds. During 1–5 June in eastern China (Nanjing, Suzhou (31.3°N, 120.6°E), Hangzhou (30.25°N, 120.167°E), and Shanghai (31.2°N, 121.5°E)), the aerosol speciation measurements indicate a large contribution of OC to

Desyaterik et al., 2013]. More results on the AAE can be found in the supporting information [Chung et al., 2012; Wang et al., 2015b; Yuan et al., 2016; Zhuang et al., 2015].

Aerosol mass extinction efficiency (MEE) is estimated from the linear regression slope between the aerosol extinction coefficient at 500 nm and PM_{2.5} mass during 1–5 June. As shown in Figure 8, the good correlation is indicated by the linear correlation coefficient of 0.82 and 0.95 under dry and wet conditions, respectively. Second, the linear slope or MEE shows strong dependence on relative humidity, increasing from 4.1 m²g⁻¹ for RH < 60% (dry) to 7.0 m²g⁻¹ for RH > 70% (wet). This indicates the strong hygroscopicity of aerosols in Nanjing City, which is probably due to the aging and mixture of smoke with urban and anthropogenic aerosols along the transport path [Li et al., 2015, 2016]. Dillner et al. [2001] found that the EC mass extinction efficiency in air shows dependence on wavelengths and particle size. For particles with diameters between 0.09 and 2.7 µm and an assumed density of 1.9 g/cm³, the measured EC mass extinction efficiency at 550 nm ranges from 7.3 to 1.7 m²g⁻¹. In addition,

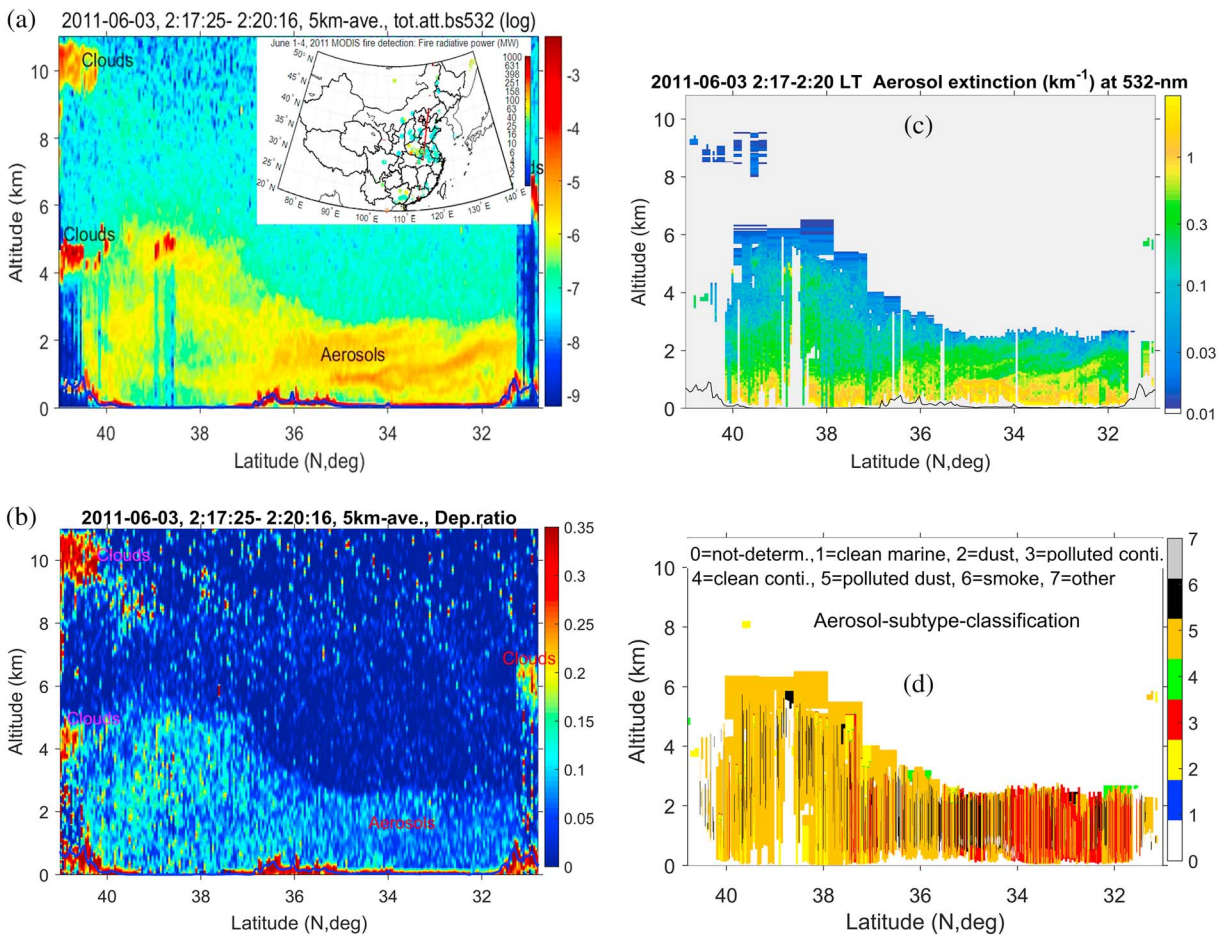


Figure 9. CALIPSO (a) attenuated backscatter, (b) total depolarization ratio, (c) aerosol extinction at 532 nm, and (d) aerosol subtype at 2:17–2:20 (nighttime) on 3 June 2011 in eastern China.

the total PM_{2.5} mass, with a few percent contribution from the soil component [Cheng *et al.*, 2014]. We note that in the CALIPSO VFM algorithm, the aerosols are classified as the polluted continental type if they are below 1 km near the surface [Omar *et al.*, 2009]. Thus, the aerosols from agricultural fire smoke near the surface are not properly classified. The CALIPSO algorithm classifies aerosol layers that have volume depolarization ratio (δ_v) greater than 0.2 as desert dust and $0.075 < \delta_v < 0.2$ as polluted dust [Omar *et al.*, 2009]. Thus, the smoke aerosols in the PBL are partially misclassified, and this may affect the retrievals of aerosol extinction since the aerosol type-dependent lidar ratios (i.e., extinction-to-backscatter ratio) are used in the CALIPSO algorithm [Omar *et al.*, 2009]. For instance, for smoke, polluted continental, polluted dust, and dust, the lidar ratios at 532 nm (1064 nm) are taken as 70 (40), 70 (30), 55 (48), and 40 (55) sr, respectively (version 3.02). With a lower lidar ratio, the aerosol extinction coefficient is generally underestimated [Kovalev, 1995].

Figure 10 gives the aerosol height distribution along the CALIPSO track in the daytime (13:19–13:22 Beijing time) on 3 June 2011 in the east coast of China. The results show that the aerosols are mostly located below 2 km altitude in the latitude zone of 30°–36°N, a little higher than the values for nighttime in Figure 9. In addition, in the north of 36°N, the aerosols can be found at 6 km altitude in Figure 10a. Again, some dense cases of aerosols are misclassified as clouds or some near-surface aerosols are not identified due to total attenuation of laser beams by the aloft dense layers or clouds as shown in Figure 10c, thus resulting in false nonretrievals of aerosol extinctions in this location in Figure 10b. The transport of ABB smoke to the ocean (e.g., Yellow Sea or East China Sea; 120°~140°E longitude) is also verified with the altitude <2 km from the CALIPSO (not shown here) during 1–5 June 2011. The aerosols in the PBL are mostly classified as polluted dust, smoke, and dust. However, according to the aerosol speciation analysis for Shanghai [Cheng *et al.*, 2014], there is

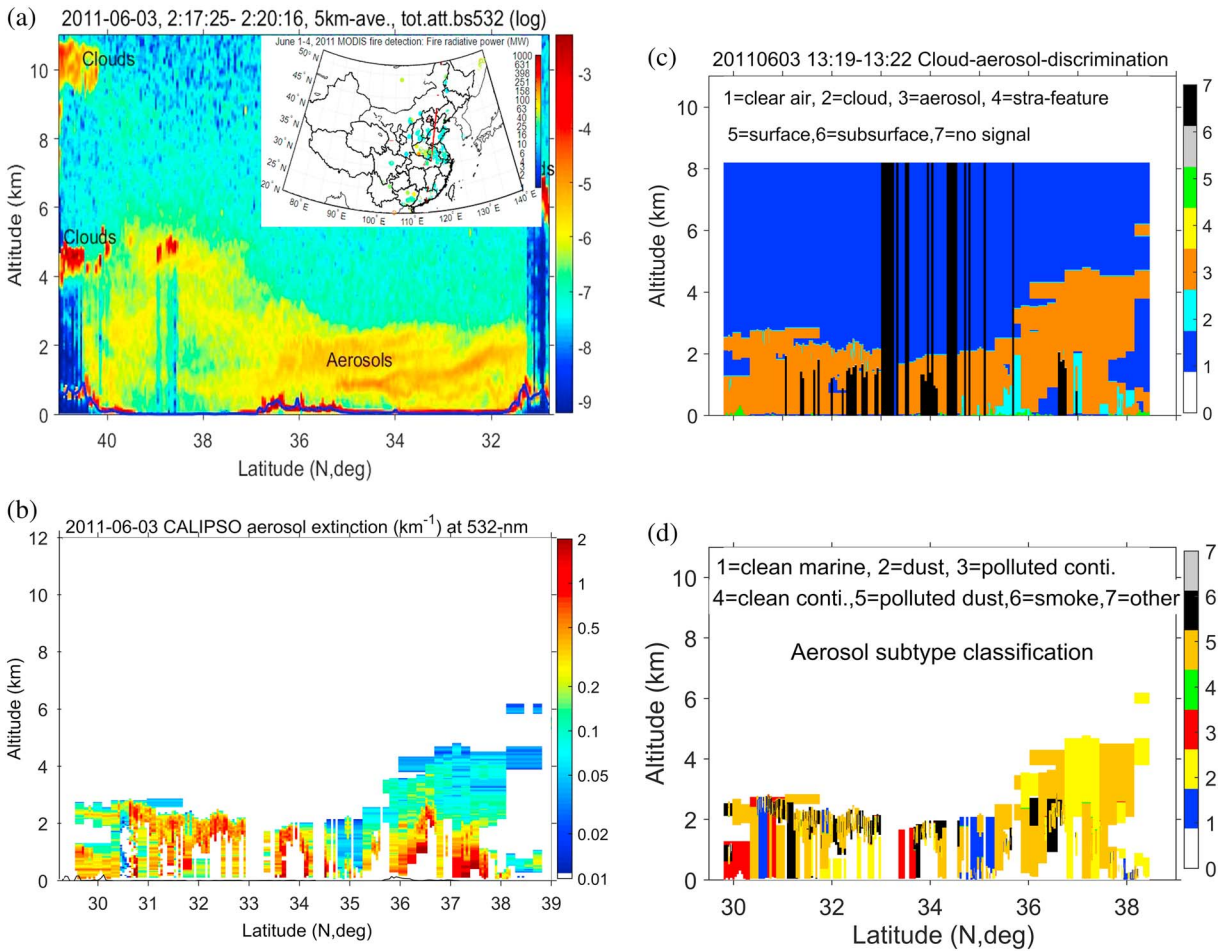


Figure 10. CALIPSO (a) attenuated backscatter, (b) aerosol extinction at 532 nm, (c) aerosol-cloud discrimination, and (d) aerosol-type classification at 13:19–13:22 (daytime) on 3 June 2011 in east China.

only a small percentage of soil component and a dominant OC component in the east coast of China. Thus, the aerosols are partially misclassified. Such misclassifications of polluted dust are generally due to the dense smoke concentrations and the multiple-scattering enhanced depolarization ratio [Burton *et al.*, 2013; Wu *et al.*, 2014].

3.5. WRF-Chem Model Evaluation

We evaluated the ground PM_{2.5} concentrations between the WRF-Chem model and our observations for this smoke event in Nanjing. At first, we compared the ground-level meteorological parameters as shown in Figure 11. Generally, the model results agree well with the ground observations in term of surface temperature, relative humidity, and wind direction. Somehow, the wind speeds from the model are much stronger than the observations, particularly in the early morning of 3–4 June when the PM_{2.5} shows the big increases. The similar positive wind bias has been reported by previous studies using WRF [Tuccella *et al.*, 2012] and may be attributed to difficulties on resolving weak winds and complex topographical features [Cheng and Steenburgh, 2005].

The hourly PM_{2.5} comparisons are shown in Figure 12. The model performance differs for the two phases of smoke intrusions, e.g., phase 1 from 20:00 of 2 June to 10:00 of 3 June and phase 2 from 20:00 of 3 June to 16:00 of 4 June. At first, for phase 1, the model data show consistent timing or temporal variation of PM_{2.5} but also slight overestimates. In phase 2, the model shows large underestimates compared to the observations. To explore this bias, the time-height distribution of PM_{2.5} and the PBL height from the model are given in Figure 13. Compared to the lidar profiles, the model data show slightly lower altitudes of aerosols in phase 1, which results in the overestimate of PM_{2.5} on the ground; this might be due to the fact that the plume-rise

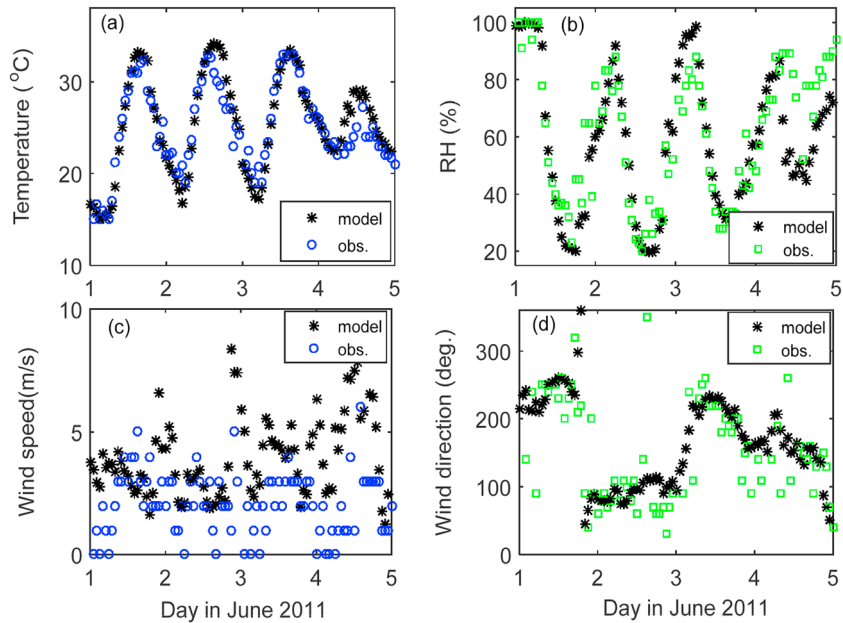


Figure 11. Comparisons of ground meteorological parameters: (a) temperature, (b) RH, (c) wind speed, and (d) wind direction.

parameterization is not used in the model. However, in phase 2, the model results show a large amount of elevated aerosols up to 3.0 km altitude, whereas the lidar profiles indicate most aerosols accumulated within 1 km. The model also shows relatively high levels of CO, OC, EC, and NO₃ and low level of SO₄ at the aloft layers (not shown here), which verify the transport of smoke. Figure 13b gives two specific vertical profiles of aerosols from the model and lidar; the model data clearly show more elevated aerosols. Figure 14 shows the spatial distribution of ground PM_{2.5} from the model in phase 1 (06:00 on 3 June) and phase 2 (00:00 on 4 June) in east China. The PM_{2.5} in Figure 14a shows consistently high concentrations in Nanjing in phase 1 that are associated with the smoke transport. However, Figure 14b indicates relatively low concentrations of PM_{2.5} in Nanjing but dense in the southwest of Nanjing in phase 2, which might be due to the misrepresentation of horizontal transport in the PBL. Furthermore, we compared the modeled wind profiles to the radiosonde observations in Figure 15 in phase 2. The model data show much stronger wind speeds in the PBL than the observation data.

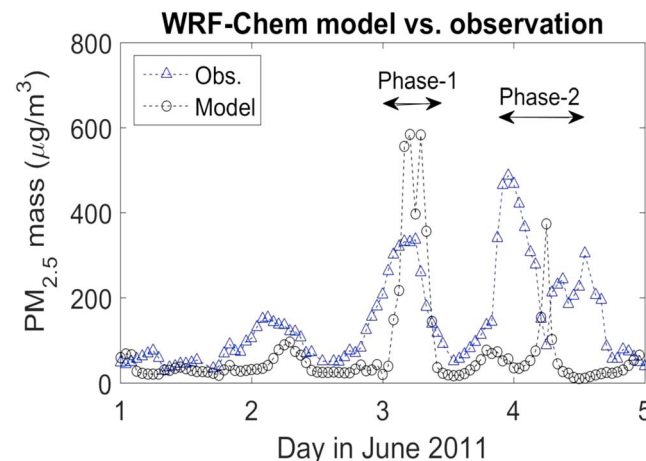


Figure 12. PM_{2.5} concentration comparison between the WRF-Chem model and observation (TEOM-1400) in Nanjing.

To further investigate the possible effects from PM_{2.5} emissions and vertical distribution, the total column PM_{2.5} ($\sum_0^{z_{top}} F(z)$) and height-scaled PM_{2.5} ($\int_0^{z_{top}} F(z) dz \times z_{top}/z_0$) concentrations are calculated, where $F(z)$ is the vertical profile of PM_{2.5} concentration, z_{top} is its top altitude, and z_0 is a scaled low altitude. The results are shown in Figure 16. High loadings of total PM_{2.5} in phase 2 can be seen, which are likely associated with the transported smoke. But, there is a few hours of time difference for the maximum PM_{2.5}, which might be due to the differences in wind speed. Interestingly, the height-scaled

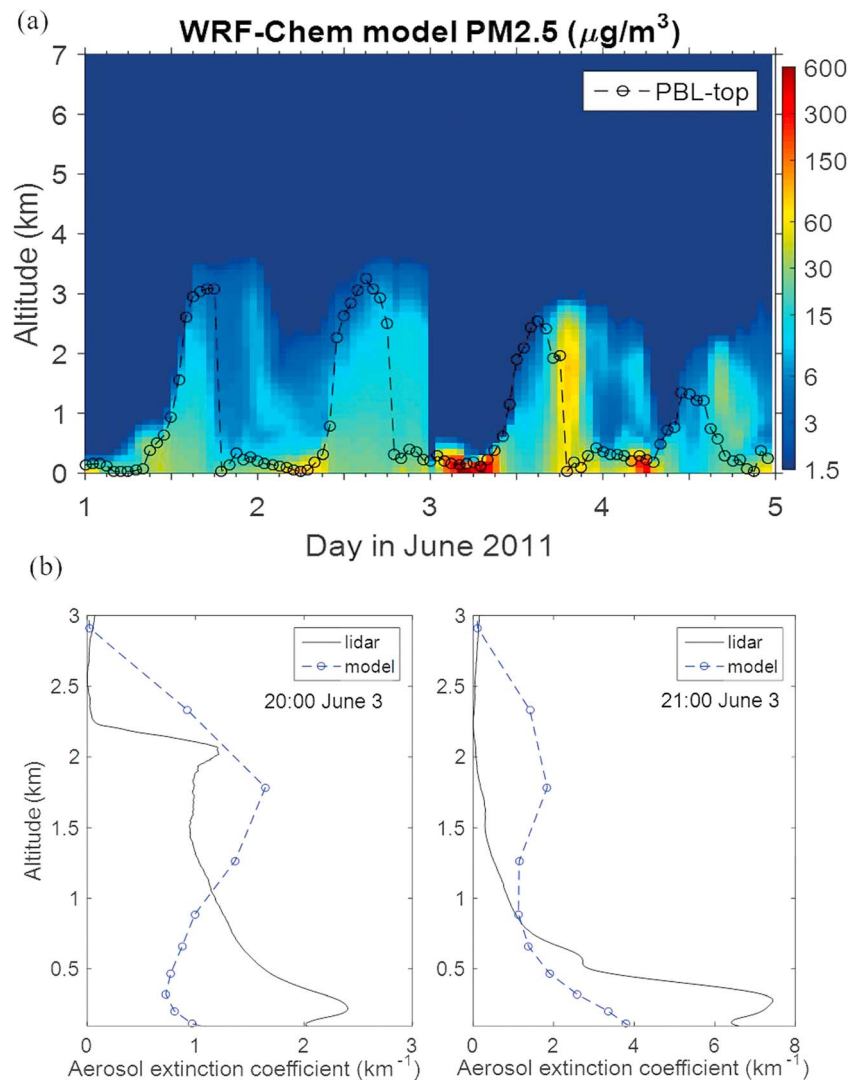


Figure 13. (a) Time-height distribution of PM_{2.5} from the model in Nanjing and (b) aerosol extinction profiles from the model and lidar on 3 June.

PM_{2.5} shows similar temporal variation and magnitude of PM_{2.5} with the observations after considering the difference of wind speeds. Thus, the improper vertical apportion and transport of aerosols or PM_{2.5} by the model probably cause the lower PM_{2.5} values on the ground in phase 2. This can be related to smoke injection height, convective transport, deposition and dispersion processes, and coarse vertical resolution of the model. In addition, we compared the WRF-Chem AOD to the available satellite MODIS-AOD under the clear sky (see Figure S3). The model AOD shows lower values than the MODIS data near the fire source region and in the downwind area, suggesting the underestimate from the fire emissions partially attributed to the cloud cover. The transport paths are generally consistent after considering their time difference (~30 min) and clouds preventing the MODIS-AOD retrievals.

Higher altitudes of wildfire smoke in the model than the observations have also been reported in the previous studies [Madden et al., 2015; Archer-Nicholls et al., 2015], which are generally associated with plume injection height, convective transport, deposition and dispersion process, vertical resolution of the model, and the assumption of a daily constant emission rates of wildfires at the same location [Val Martin et al., 2012; Colarco et al., 2004; Kipling et al., 2016]. Having aerosol injected into the wrong portion of the vertical column can have many implications; e.g., it can impact the simulated ground-level air quality [Colarco et al., 2004] and the atmospheric heating rates at different altitudes. Our study

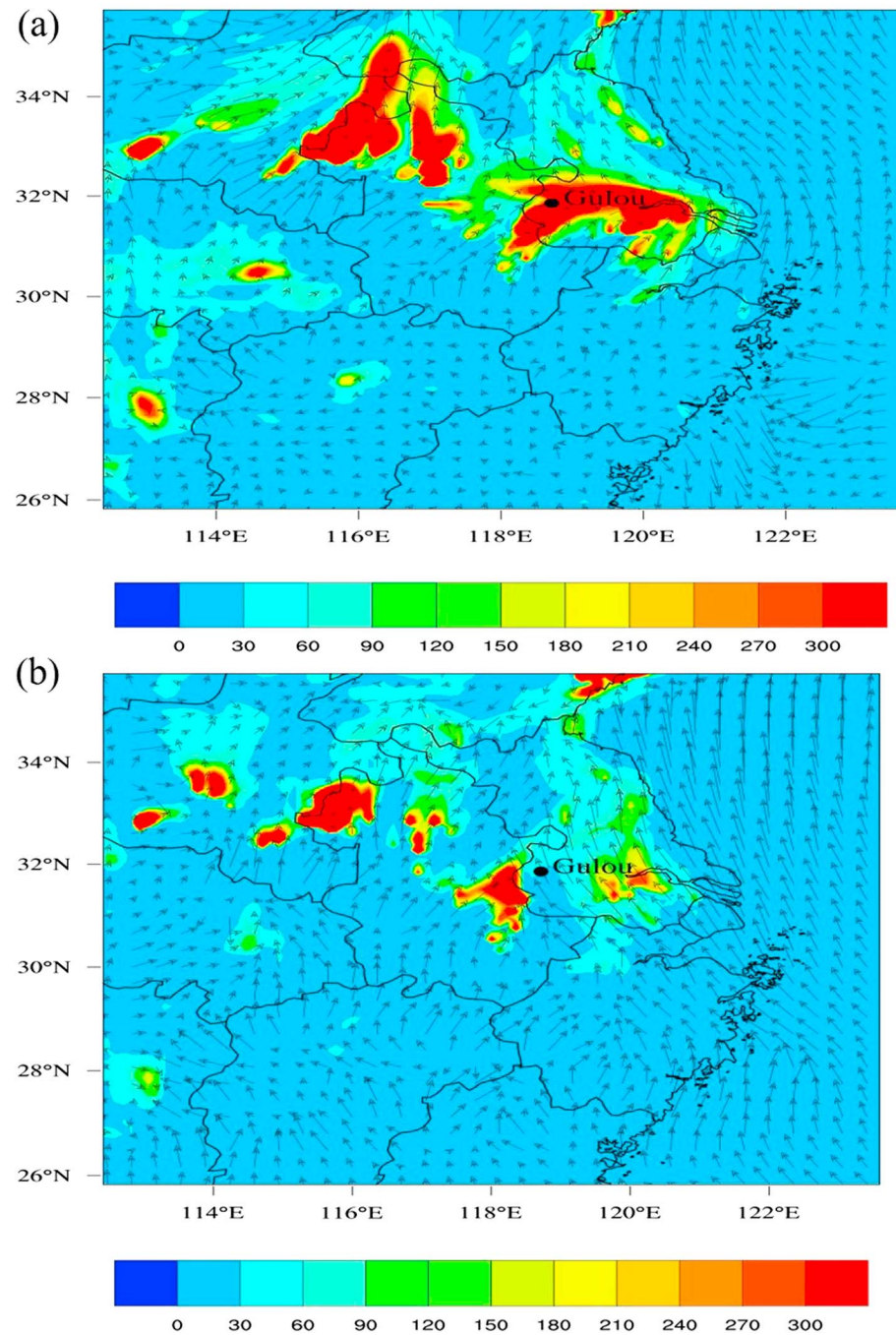


Figure 14. Spatial distribution of ground PM_{2.5} ($\mu\text{g}/\text{m}^3$) and wind direction from the model at (a) 6:00, 3 June 2011 (phase 1) and (b) 00:00, 4 June 2011 (phase 2). Black dot: Nanjing-Gulou site.

indicates that the vertical distribution of transported smoke may be improper in the model. Thus, the assimilation or validation with aerosol vertical profiles would help improve the model forecast of ground-level PM_{2.5}.

Since the observed PM_{2.5} includes all the emissions from the anthropogenic sources and agricultural fires smoke, it is difficult to isolate the smoke contribution using observations. By switching on and off the ABB emissions in the model, we can simulate the fractional contribution of transported smoke to total PM_{2.5}. The daily average results on 3–4 June are given in Figure 17. It can be seen that over the 2 days the transported ABB smoke can contribute to 50–70% of the total PM_{2.5} in Nanjing (32.05°E, 118.7°E).

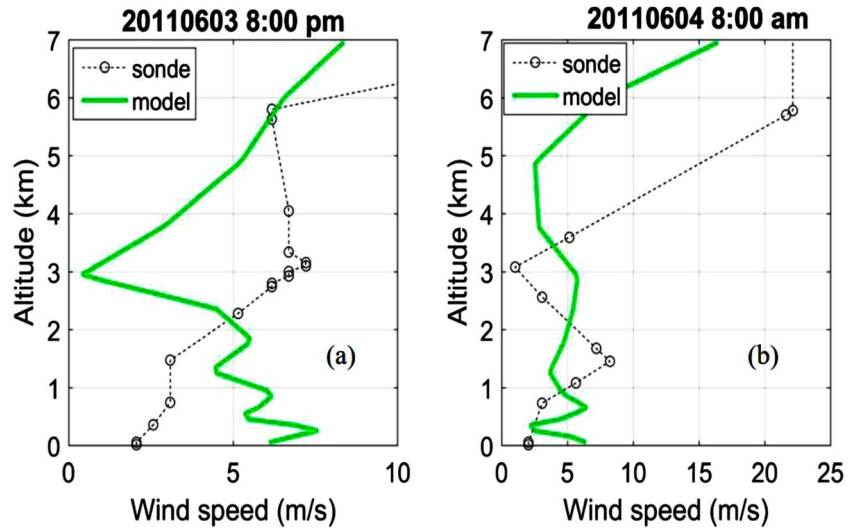


Figure 15. Wind profiles from the model and radiosonde at (a) 08:00 P.M. on 3 June and (b) 08:00 A.M. on 4 June.

4. Conclusions

The synergistic observations from a ground-based lidar, Sun photometer, and in situ and satellite sensors of an agriculture biomass burning episode in eastern China are presented and compared to the WRF-Chem model results. The time-height distribution, optical properties, sources, long-range transport of smoke aerosols, and their strong impacts on air quality are analyzed. The results indicate that smoke aerosols are mainly located in the PBL (<1.5 km) and have a small depolarization ratio (<0.08) on 3–4 June 2011. The transported smoke leads to very high AOD (~3.0 at 500 nm), large Angstrom exponent of 1.6, and relatively small SSA of 0.8–0.9 at 440–1020 nm, indicating the existence of fine-mode absorbing aerosols. The absorption Angstrom exponent shows a value smaller than 1.0 that may be due to the coating or mixture of aged smoke with urban aerosols. Importantly, during the smoke intrusion period, the ground PM₁₀ and PM_{2.5} concentrations show a significant and consistent increase, with the peak value of 800 μg/m³ and 485 μg/m³, respectively. Stagnant and high-moisture weather leads to the transported and local aerosols accumulating near the surface, thus resulting in heavy air pollution. The sources from agricultural fires are identified in the region between 30°–37°N latitude and 110°–120°E longitude (e.g., Jiangshu, Anhui, and Henan Provinces) from the MODIS fire and CALIPSO aerosol products. Meanwhile,

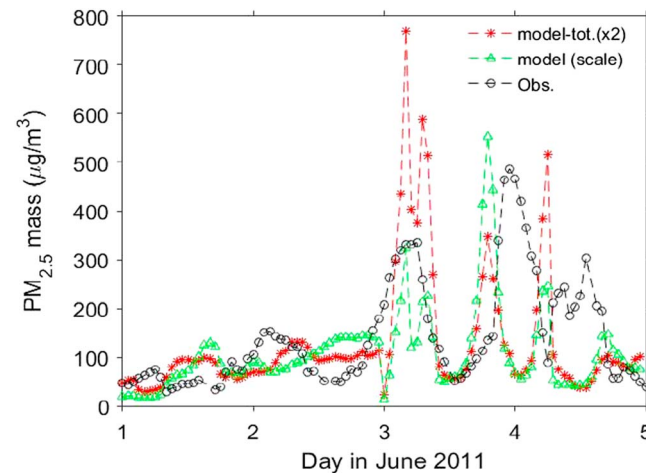


Figure 16. Total column PM_{2.5} (×2), height-scaled PM_{2.5} from the WRF-Chem model and observations.

the aerosol mass extinction efficiency shows an enhancement with relative humidity due to the strong hygroscopic properties of the aerosols observed. The ground PM_{2.5} shows a good correlation with the AOD due to the fact that the aerosol pollution is mostly confined in the PBL. The range-resolved CALIPSO measurements illustrate that the aerosols are mostly loaded in the PBL in eastern China and transported to the ocean (Yellow Sea and East China Sea). Some dense smoke is misclassified as clouds or polluted dust in the CALIPSO product, which in turn affects the retrieval accuracy of aerosol extinction due to the type-dependent lidar ratio used. Finally, the WRF-Chem model shows a

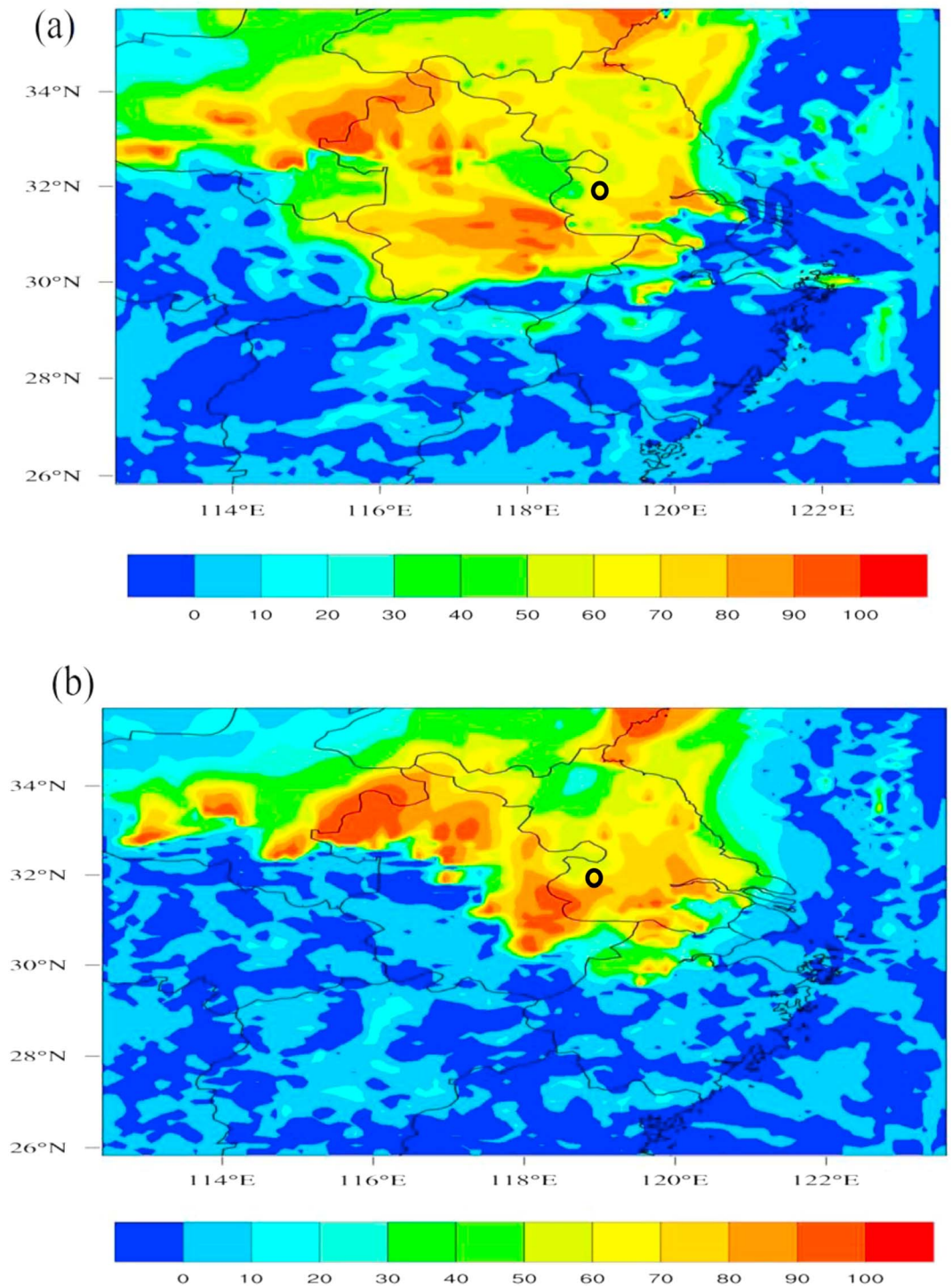


Figure 17. Fractional contribution (%) of smoke to the total $PM_{2.5}$ from the WRF-Chem model on (a) 3 June 2011 and (b) 4 June 2011. Black-circle: Nanjing-Gulou site.

consistent increasing tendency of ground $PM_{2.5}$ in phase 1 (from 20:00 of 2 June to 10:00 on 3 June) but dramatic underestimates for phase 2 (from 20:00 on 3 June to 16:00 on 4 June) when dense aerosols are present. Such discrepancy is associated with the improper vertical apportionment of transported smoke, atmospheric diffusion conditions, and misrepresentation of the horizontal transport in the PBL in the model.

Acknowledgments

Y. Wu is supported by the research project of NOAA NA11SEC4810004. In addition, this work was jointly supported by the National Science and Technology Major Project (grant 2016YFC0203303), the National Science Foundation of Jiangsu Province (grant BE2015151), the National Science Foundation of China (grants 41075012, 40805006, 91544230, and 41575145), and the National Special Fund for Environmental Protection Research in the Public Interest (grant 201409008). Also, Y.H., M.X., and A.V. wish to thank the European Commission's Marie Curie Actions International Research Staff Exchange Scheme for funding Y.H.'s and M.X.'s placements at Imperial College London and thus facilitating interactions with A.V. on this work, as part of the Regional Climate-Air Quality Interactions project (PIRSES-GA-2013-612671). Special thanks to Zhen Cheng from Shanghai Jiaotong University for providing the aerosol species data. We appreciate Gan Luo from Atmospheric Sciences Research Center, the State University of New York at Albany, and Xin Huang from School of Atmospheric Sciences, Nanjing University, for the discussions of WRF-Chem model results. We also gratefully acknowledged the constructive comments from the anonymous reviewers that greatly improve the manuscript. The CALIPSO data can be obtained from the Atmospheric Data Center at NASA Langley (<https://eosweb.larc.nasa.gov/project/calipso>). The MODIS, OMI, and AIRS data are provided by NASA GES DISC through the website <http://disc.sci.gsfc.nasa.gov/>. The NCEP Reanalysis data were provided by the NOAA-ESRL, Boulder, CO, USA, from <http://www.esrl.noaa.gov/psd/>. The HYSPLIT data are from the NOAA Air Resources Laboratory (<http://ready.arl.noaa.gov>). The data in this paper can be made available to other researchers through correspondence with Yong Han (HanYong@nju.edu.cn).

References

- Ackerman, A. S., O. B. Toon, D. E. Stevens, A. J. Heymsfield, V. V. Ramanathan, and E. J. Welton (2000), Reduction of tropical cloudiness by soot, *Science*, *288*, 1042–1047.
- Alexander, D. T. L., P. A. Crozier, and J. R. Anderson (2008), Brown carbon spheres in East Asian outflow and their optical properties, *Science*, *321*, 833–836.
- Andreae, M. O., D. Rosenfeld, P. Artaxo, A. A. Costa, G. P. Frank, K. M. Longo, and M. A. F. Silva-Dias (2004), Smoking rain clouds over the Amazon, *Science*, *303*, 1337–1342.
- Archer-Nicholls, S., et al. (2015), Characterizing Brazilian biomass burning emissions using WRF-Chem with MOSAIC sectional aerosol, *Geosci. Model Dev.*, *8*, 549–577.
- Bahadur, R., P. Praveen, Y. Xu, and V. Ramanathan (2012), Solar absorption by elemental and brown carbon determined from spectral observations, *Proc. Natl. Acad. Sci. U.S.A.*, *109*(43), 17,366–17,371.
- Berge, E., H. C. Huang, J. Chang, and T. H. Liu (2001), A study of the importance of initial conditions for photochemical oxidant modeling, *J. Geophys. Res.*, *106*(D1), 1347–1363, doi:10.1029/2000JD900227.
- Bergstrom, R. W., P. B. Russell, and P. Hignett (2002), Wavelength dependence of the absorption of black carbon particles: Predictions and results from the TARFOX experiment and implications for the aerosol single scattering albedo, *J. Atmos. Sci.*, *59*, 567–577.
- Bergstrom, R. W., P. Pilewskie, P. B. Russell, J. Redemann, T. C. Bond, P. K. Quinn, and B. Sierau (2007), Spectral absorption properties of atmospheric aerosols, *Atmos. Chem. Phys.*, *7*, 5937–5943.
- Boersma, K., E. Bucsela, E. Brinksma, and J. Gleason (2001), NO₂, OMI-EOS algorithm, Theoretical Basis Document: Trace gas algorithms: NO₂, *4*, 12–35.
- Bond, T. C., and R. W. Bergstrom (2006), Light absorption by carbonaceous particles: An investigative review, *Aerosol Sci. Technol.*, *40*, 27–67.
- Burton, S. P., R. A. Ferrare, M. A. Vaughan, A. H. Omar, R. R. Rogers, C. A. Hostetler, and J. W. Hair (2013), Aerosol classification from airborne HSRL and comparisons with the CALIPSO vertical feature mask, *Atmos. Meas. Tech.*, *6*, 1397–1412.
- Chen, Y. X., B. Zhu, C. Yi, X. W. Hou, H. L. Wang, H. Q. Kang, and X. H. Liu (2014), A continuous air pollution event in Jiangshu and Anhui Province based on satellite remote sensing and filed observations, *China Environ. Sci.*, *34*(4), 827–836.
- Cheng, W. Y., and W. J. Steenburgh (2005), Evaluation of surface sensible weather forecasts by the WRF and the Eta models over the western United States, *Weather Forecast.*, *20*, 812–821.
- Cheng, Z., et al. (2014), Impact of biomass burning on haze pollution in the Yangtze River delta, China: A case study in summer 2011, *Atmos. Chem. Phys.*, *14*, 4573–4585.
- Chou, M. D., and M. J. Suarez (1999), A shortwave radiation parameterization for atmospheric studies NASA/TM-104606, vol. 15, 40.
- Chung, C. E., S. W. Kim, M. Lee, S. C. Yoon, and S. Lee (2012), Carbonaceous aerosol AAE inferred from in-situ aerosol measurements at the Gosan ABC super site, and the implications for brown carbon aerosol, *Atmos. Chem. Phys.*, *12*, 6173–6184.
- Colarco, P. R., M. R. Schoeber, B. G. Doddridge, L. T. Marufu, O. Torres, and E. J. Welton (2004), Transport of smoke from Canadian forest fires to the surface near Washington, D.C.: Injection height, entrainment, and optical properties, *J. Geophys. Res.*, *109*, D06203, doi:10.1029/2003JD004248.
- Desyaterik, Y., Y. Sun, X. Shen, T. Lee, X. Wang, T. Wang, and J. L. Collett Jr. (2013), Speciation of “brown” carbon in cloud water impacted by agricultural biomass burning in eastern China, *J. Geophys. Res. Atmos.*, *118*, 7389–7399, doi:10.1002/jgrd.50561.
- Dillner, A. M., C. Stein, S. M. Larson, and R. Hitznerberger (2001), Measuring the mass extinction efficiency of elemental carbon in rural aerosol, *Aerosol Sci. Technol.*, *35*(6), 1009–1021.
- Draxler, R. R., and G. D. Hess (1997), Description of the HYSPLIT_4 modeling system NOAA Tech. Memo. ERL ARL-224, NOAA Air Resources Laboratory, Silver Spring, MD, 24.
- Dubovik, O., and M. D. King (2000), A flexible inversion algorithm for retrieval of aerosol optical properties from Sun and sky radiance measurements, *J. Geophys. Res.*, *105*(D16), 20,673–20,696, doi:10.1029/2000JD900282.
- Ek, M. B., K. E. Mitchell, Y. Lin, E. Rogers, P. Grunmann, V. Koren, G. Gayno, and J. D. Tarpley (2003), Implementation of Noah land surface model advances in the National Centers for Environmental Prediction operational mesoscale Eta model, *J. Geophys. Res.*, *108*(D22), 8851, doi:10.1029/2002JD003296.
- Gallus, W. A., and J. F. Bresch (2006), Comparison of impacts of WRF dynamic core, physics package, and initial conditions on warm season rainfall forecasts, *Mon. Weather Rev.*, *134*(9), 2632–2641, doi:10.1175/MWR3198.1.
- Garg, S., B. Chandra, and V. Sinha (2016), Limitation of the use of the absorption Angstrom exponent for source apportionment of equivalent black carbon: A case study from the northwest Indo-Gangetic Plain, *Environ. Sci. Technol.*, *50*, 814–824.
- Giglio, L., I. Csizsar, and C. Justice (2006), Global distribution and seasonality of active fires as observed with Terra and Aqua Moderated Resolution Imaging Spectroradiometer (MODIS) sensors, *J. Geophys. Res.*, *111*, G02016, doi:10.1029/2005JG000142.
- Giles, D. M., B. N. Holben, T. F. Eck, A. Sinyuk, A. Smirnov, I. Slutsker, R. R. Dickerson, A. M. Thompson, and J. S. Schafer (2012), An analysis of AERONET aerosol absorption properties and classifications representative of aerosol source regions, *J. Geophys. Res.*, *117*, D17203, doi:10.1029/2012JD018127.
- Grell, G. A., and D. Devenyi (2002), A generalized approach to parameterizing convection combining ensemble and data assimilation techniques, *Geophys. Res. Lett.*, *29*(14), 1693, doi:10.1029/2002GL015311.
- Grell, G. A., S. E. Peckham, R. Schmitz, S. A. McKeen, G. Frost, W. C. Skamarock, and B. Eder (2005), Fully coupled “online” chemistry within the WRF model, *Atmos. Environ.*, *39*, 6957–6975.
- Guenther, A., T. Karl, P. Harley, C. Wiedinmyer, P. I. Palmer, and C. Geron (2006), Estimates of global terrestrial isoprene emissions using MEGAN (Model of Emissions of Gases and Aerosols from Nature), *Atmos. Chem. Phys.*, *6*, 3181–3210.
- Han, Y., Y. Wu, T. Wang, C. Xie, K. Zhao, B. Zhuang, and S. Li (2015a), Characterizing a persistent Asian dust transport event: Optical properties and impact on air quality through the ground-based and satellite measurements over Nanjing, China, *Atmos. Environ.*, *115*, 304–316.
- Han, Y., Y. Wu, T. Wang, B. Zhuang, S. Li, and K. Zhao (2015b), Impacts of elevated-aerosol-layer and aerosol type on the correlation of AOD and particulate matter with ground-based and satellite measurements in Nanjing, southeast China, *Sci. Total Environ.*, *532*, 195–207.
- Hand, J. L., and W. C. Malm (2007), Review of aerosol mass scattering efficiencies from ground-based measurements since 1990, *J. Geophys. Res.*, *112*, D16203, doi:10.1029/2007JD008484.
- Hoff, R. M., and S. A. Christopher (2009), Remote sensing of particulate pollution from space: Have we reached the promised land, *J. Air Waste Manage. Assoc.*, *59*, 645–675.
- Holben, B. N., et al. (1998), AERONET—A federated instrument network and data archive for aerosol characterization, *Remote Sens. Environ.*, *66*, 1–16.

- Horvath, H., and K. E. Noll (1969), The relationship between atmospheric light scattering coefficient and visibility, *Atmos. Environ.*, *3*(5), 543–550.
- Huang, X., M. M. Li, J. F. Li, and Y. Song (2012), A high-resolution emission inventory of crop burning in fields in China based on MODIS thermal anomalies/fire products, *Atmos. Environ.*, *50*, 9–15.
- Huang, X., T. J. Wang, F. Jiang, J. B. Liao, Y. F. Cai, C. Q. Yin, J. L. Zhu, and Y. Han (2013), Studies on a severe dust storm in East Asia and its impact on the air quality of Nanjing, China, *Aerosol Air Qual. Res.*, *13*, 179–193.
- Johnson, B. T., K. P. Shine, and P. M. Forster (2004), The semi-direct aerosol effect: Impact of absorbing aerosols on marine stratocumulus, *Q. J. R. Meteorol. Soc.*, *130*(599), 1407–1422.
- Kipling, Z., et al. (2016), What controls the vertical distribution of aerosol? Relationships between process sensitivity in HadGEM3–UKCA and inter-model variation from AeroCom phase II, *Atmos. Chem. Phys.*, *16*, 2221–2241.
- Koren, I., Y. J. Kaufman, L. A. Remer, and J. V. Martins (2004), Measurement of the effect of Amazon smoke on inhibition of cloud formation, *Science*, *303*(5662), 1342–1345.
- Koren, I., J. V. Martins, L. A. Remer, and H. Fargan (2008), Smoke invigoration versus inhibition of clouds over the Amazon, *Science*, *321*, 946–949.
- Kovalev, V. A. (1995), Sensitivity of the lidar solution to errors of the aerosol backscatter-to-extinction ratio: Influence of a monotonic change in the aerosol extinction coefficient, *Appl. Opt.*, *34*, 3457–3462.
- Lack, D. A., and C. D. Cappa (2010), Impact of brown and clear carbon on light absorption enhancement, single scatter albedo and absorption wavelength dependence of black carbon, *Atmos. Chem. Phys.*, *10*, 4207–4220.
- Lack, D. A., J. M. Langridge, R. Bahreini, C. D. Cappa, A. M. Middlebrook, and J. P. Schwarz (2012), Brown carbon and internal mixing in biomass burning particles, *Proc. Natl. Acad. Sci. U.S.A.*, *109*(37), 14,802–14,807.
- Levy, R. C., L. A. Remer, and O. Dubovik (2007), Global aerosol optical properties and application to Moderate Resolution Imaging Spectroradiometer aerosol retrieval over land, *J. Geophys. Res.*, *112*, D13210, doi:10.1029/2006JD007815.
- Li, C., Z. Ma, J. Chen, X. Wang, X. Ye, L. Wang, X. Yang, H. Kan, D. J. Donaldson, and A. Mellouki (2015), Evolution of biomass burning smoke particles in the dark, *Atmos. Environ.*, *120*, 244–252.
- Li, C., Y. Hu, J. Chen, Z. Ma, X. Ye, X. Yang, L. Wang, X. Wang, and A. Mellouki (2016), Physicochemical properties of carbonaceous aerosol from agricultural residue burning: Density, volatility, and hygroscopicity, *Atmos. Environ.*, *140*, 94–105.
- Li, H. Y., Z. Han, T. Cheng, H. Du, L. Kong, J. Chen, R. Zhang, and W. Wang (2010), Agricultural fire impacts on the air quality of Shanghai during summer harvest time, *Aerosol Air Qual. Res.*, *10*(2), 95–101.
- Lin, Y. L., R. D. Farley, and H. D. Orville (1983), Bulk parameterization of the snow field in a cloud model, *J. Clim. Appl. Meteorol.*, *22*(6), 1065–1092.
- Lu, X. B., Y. Y. Yu, Y. Fu, Y. Zhang, Y. Mu, and Z. Cheng (2014), Characterization and identification method of ambient air quality influenced by straw burning, *Environ. Monit. Manage. Tech.*, *26*(4), 17–21.
- Madden, J., N. Mölders, and K. Sassen (2015), Assessment of WRF/Chem simulated vertical distributions of particulate matter from the 2009 Minto Flats South wildfire in interior Alaska by CALIPSO total backscatter and depolarization measurements, *Open J. Air Pollut.*, *4*, 119–138.
- Monin, A. S., and A. M. Obukhov (1954), Basic laws of turbulent mixing in the surface layer of the atmosphere, *Tr Akad Nauk SSSR Geophys. Inst.*, *24*(151), 163–187.
- National Research Council (2009), *Global Sources of Local Pollution: An Assessment of Long-Range Transport of Key Air Pollutants to and From the United States*, The National Academies Press, Washington, D. C.
- Ni, H., et al. (2015), Emission characteristics of carbonaceous particles and trace gases from open burning of crop residues in China, *Atmos. Environ.*, *123*, 399–406.
- Noh, Y., W. G. Cheon, S. Y. Hong, and S. Raasch (2003), Improvement of the K-profile model for the planetary boundary layer based on large eddy simulation data, *Boundary-Layer Meteorol.*, *107*(2), 401–427, doi:10.1023/A:1022146015946.
- Omar, A., et al. (2009), The CALIPSO automated aerosol classification and lidar ratio selection algorithm, *J. Atmos. Oceanic Technol.*, *26*, 1994–2014.
- Pan, L., H. Che, F. Geng, X. Xia, Y. Wang, C. Zhu, M. Chen, W. Gao, and J. Guo (2010), Aerosol optical properties based on ground measurements over the Chinese Yangtze Delta Region, *Atmos. Environ.*, *44*, 2587–2596.
- Qu, C., B. Li, H. Wu, and J. P. Giesy (2012), Controlling air pollution from straw burning in China calls for efficient recycling, *Environ. Sci. Technol.*, *46*, 7934–7936.
- Russell, P. B., R. W. Bergstrom, Y. Shinozuka, A. D. Clarke, P. F. DeCarlo, J. L. Jimenez, J. M. Livingston, J. Redemann, O. Dubovik, and A. Strawa (2010), Absorption Angstrom exponent in AERONET and related data as an indicator of aerosol composition, *Atmos. Chem. Phys.*, *10*, 1155–1169.
- Sassen, K. (1991), The polarization lidar technique for cloud research: A review and current assessment, *Bull. Am. Meteorol. Soc.*, *72*, 1848–1866.
- Sato, M., J. Hansen, D. Koch, A. Lacis, R. Ruedy, O. Dubovik, B. Holben, M. Chin, and T. Novakov (2003), Global atmospheric black carbon inferred from AERONET, *Proc. Natl. Acad. Sci. U.S.A.*, *100*(11), 6319–6324.
- Streets, D., Yarber K., Woo J., and Carmichael K. (2003), Biomass burning in Asia: Annual and seasonal estimates and atmospheric emissions, *Global Biogeochem. Cycles*, *17*(4), 1099, doi:10.1029/2003GB002040.
- Susskind, J., C. Barnet, and J. Blaisdell (2003), Retrieval of atmospheric and surface parameters from AIRS/AMSU/HSB data in the presence of clouds, *IEEE Geosci. Remote Sens.*, *2*, 390–409.
- Tuccella, P., G. Curci, G. Visconti, B. Bessagnet, and L. Menut (2012), Modeling of gas and aerosol with WRF/Chem over Europe: Evaluation and sensitivity study, *J. Geophys. Res.*, *117*, D03303, doi:10.1029/2011JD016302.
- Val Martin, M., R. A. Kahn, J. A. Logan, R. Paugam, M. Wooster, and C. Ichoku (2012), Space-based observational constraints for 1-D fire smoke plume-rise models, *J. Geophys. Res.*, *117*, D22204, doi:10.1029/2012JD018370.
- Voulgarakis, A., and R. D. Field (2015), Fire influences on atmospheric composition, air quality, and climate, *Curr. Pollut. Rep.*, doi:10.1007/s40726-015-0007-z.
- Voulgarakis, A., M. E. Marlier, G. Faluvegi, D. T. Shindell, K. Tsigaridis, and S. Mangeon (2015), Interannual variability of tropospheric trace gases and aerosols: The role of biomass burning emissions, *J. Geophys. Res. Atmos.*, *120*, 7157–7173, doi:10.1002/2014JD022926.
- Wang, L. L., J. Xin, L. Xylem, and W. Yang (2015a), The variability of biomass burning and its influence on regional aerosol properties during the wheat harvest season in north China, *Atmos. Res.*, *157*, 153–163.
- Wang, S. H., et al. (2015b), Vertical distribution and columnar optical properties of springtime biomass-burning aerosols over northern Indochina during 2014 7-SEAS campaign, *Aerosol Air Qual. Res.*, *15*(5), 2037–2050.

- Wang, T. J., F. Jiang, J. J. Deng, Y. Shen, Q. Fu, Q. Wang, Y. Fu, J. Xu, and D. Zhang (2012), Urban air quality and regional haze weather forecast for Yangtze River Delta region, *Atmos. Environ.*, *58*, 70–83.
- Winker, D. M., M. A. Vaughan, A. Omar, Y. Hu, K. A. Powell, Z. Liu, W. H. Hunt, and S. A. Young (2009), Overview of the CALIPSO mission and CALIOP data processing algorithms, *J. Atmos. Oceanic Technol.*, *26*, 2310–2323.
- Wu, Y., C. Gan, L. Cordero, B. Gross, F. Moshary, and S. Ahmed (2010), PBL-height retrievals from the CALIOP/CALIPSO and comparison with the ground-based lidar and radiosonde measurements, *Proc. SPIE*, 78320, doi:10.1117/12.865146.
- Wu, Y., L. Cordero, B. Gross, F. Moshary, and S. Ahmed (2012), Smoke plume optical properties and transport observed by a multi-wavelength lidar, Sun photometer and satellite, *Atmos. Environ.*, *63*, 32–42.
- Wu, Y., L. Cordero, B. Gross, F. Moshary, and S. Ahmed (2014), Assessment of CALIPSO attenuated backscatter and aerosol retrievals with a combined ground-based multiwavelength lidar and Sun photometer measurement, *Atmos. Environ.*, *84*, 44–53.
- Wu, Y., P. Yan, P. Tian, J. Tao, L. Li, J. Chen, Y. Zhang, N. Cao, C. Chen, and R. Zhang (2015), Spectral light absorption of ambient aerosols in urban Beijing during summer: An intercomparison of measurements from a range of instruments, *Aerosol Air Qual. Res.*, *15*, 1178–1187.
- Xia, X., X. Zong, and L. Sun (2013), Exceptionally active agricultural fire season in mid-eastern China in June 2012 and its impact on the atmospheric environment, *J. Geophys. Res. Atmos.*, *118*, 9889–9900, doi:10.1002/jgrd.50770.
- Xie, C., T. Nishizawa, N. Sugimoto, I. Matsui, and Z. F. Wang (2008), Characteristics of aerosol optical properties in pollution and Asian dust episodes over Beijing, China, *Appl. Opt.*, *47*(27), 4945–4951.
- Xie, M., J. Liao, K. Twang, B. Zhuang, Y. Han, M. Li, and S. Li (2015), Modeling of the anthropogenic heat flux and its effect on air quality over the Yangtze River Delta region, China, *Atmos. Chem. Phys. Discuss.*, *15*, 32,367–32,412.
- Yan, X., T. Ohara, and H. Akimoto (2006), Bottom-up estimate of biomass burning in mainland China, *Atmos. Environ.*, *40*, 5362–5273.
- Yuan, J. F., X. F. Huang, L. M. Cao, J. Cui, Q. Zhu, C. N. Huang, Z. J. Lan, and L. Y. He (2016), Light absorption of brown carbon aerosol in the PRD region of China, *Atmos. Chem. Phys.*, *16*, 1433–1443.
- Zaveri, R. A., R. C. Easter, J. D. Fast, and L. K. Peters (2008), Model for Simulating Aerosol Interactions and Chemistry (MOSAIC), *J. Geophys. Res.*, *113*, D13204, doi:10.1029/2007JD008782.
- Zaveri, R. A., and L. K. Peters (1999), A new lumped structure photochemical mechanism for large-scale applications, *J. Geophys. Res.*, *104*, 30,387–30,415, doi:10.1029/1999JD900876.
- Zha, S., S. Zhang, T. Cheng, J. Chen, G. Huang, X. Li, and Q. Wang (2013), Agricultural fires and their potential impacts on regional air quality over China, *Aerosol Air Qual. Res.*, *13*, 992–1001.
- Zhang, T., M. J. Wooster, D. C. Green, and B. Main (2015), New field-based agricultural biomass burning trace gas, PM_{2.5}, and black carbon emission ratios and factors measured in situ at crop residue fires in eastern China, *Atmos. Environ.*, *121*, 22–34.
- Zhu, J. L., T. J. Wang, L. Xing, Q. Hu, and D. Zhou (2011), Analysis on the characteristic and mechanism of a heavy haze episode in Jiangsu Province, *China Environ. Sci.*, *31*(12), 1943–1950.
- Zhuang, B. L., et al. (2014), Optical properties and radiative forcing of urban aerosols in Nanjing, China, *Atmos. Environ.*, *83*, 43–52.
- Zhuang, B. L., et al. (2015), Absorption coefficient of urban aerosol in Nanjing, west Yangtze River Delta, China, *Atmos. Chem. Phys.*, *15*, 13,633–13,646.